Electronic Supplementary Information (ESI) for

Bending two-Dimensional Cu(I)-based coordination networks to inverse electrocatalytic HER/CO_2RR selectivity

Kai Zheng,[‡a] Ding-Yi Hu,[‡a] Xue-Wen Zhang,[a] Xian-Xian Xiao,[a] Zi-Jun Liang,[a] Jun-Xi Wu,[a] Duo-Yu Lin,[a] Lin-Ling Zhuo,[a] Heng Yi,[a] Li Gong,[b] Dong-Dong Zhou,[*a] and Jie-Peng Zhang[*a]

[a] MOE Key Laboratory of Bioinorganic and Synthetic Chemistry, School of Chemistry, GBRCE for Functional Molecular Engineering, IGCME, Sun Yat-Sen University, Guangzhou 510275, China

[b] Instrumental Analysis and Research Center, Sun Yat-Sen University, Guangzhou 510275, China

‡ These authors contributed equally to this work.

* Corresponding Authors: zhoudd3@mail.sysu.edu.cn; zhangjp7@mail.sysu.edu.cn

Table of Contents

Experimental Procedures

Materials and methods. All reagents were commercially available and used without further purification. Elemental analyses (EA) were performed by a Vario EL elemental analyzer. Powder X-ray diffraction (PXRD) was performed on a D8 DAVANCI X-ray powder diffractometer (Cu Kα). ^{1}H-nuclear magnetic resonance (^{1}H-NMR) spectra were recorded on a Bruker BioSpin GmbH (400 MHz). Transmission electron microscopy (TEM) or High-resolution transmission electron microscope (HRTEM) images were recorded on a JEOL ARM200F microscope. Atomic force microscopy (AFM) images were obtained by a Bruker Dimension Fastscan SPM device. X-ray photoelectron spectroscopy (XPS) was performed on an ESCA Lab250 X-ray microprobe. Operando attenuated total reflection Fourier transform infrared spectroscopy (operando ATR-FTIR) experiments were performed on a Nicolet iS50 FTIR Thermo Fisher spectrometer. Contact angles were measured using a Krüss, DSA100S goniometer.

Synthesis of [Cu(tz)] (Htz = 1,2,4-triazole). Methanol (MeOH) solution of Htz (0.02 mol L^{-1}, 50 mL) was dropped into an aqueous ammonia (25%) solution of $[Cu(NH_3)_2]OH$ (0.1 mol L^{-1}, 25 mL) under N_2 atmosphere with stirring at room temperature for 1 h. The precipitate was filtered, washed, and dried under vacuum to give white microcrystalline product (yield ~70%). Element analysis (EA) for [Cu(tz)] ($C_2H_2N_3Cu$): C 18.25, H 1.53, N 31.93; found: C 18.24, H 1.35, N 31.79.

Synthesis of [Cu(atz)] (Hatz = 3-amino-1,2,4-triazole). The same reaction methods for [Cu(tz)] were used except that Htz was replaced by Hatz (yield ~80%). EA for [Cu(atz)] ($C_2H_3N_4Cu$): C 16.38, H 2.06, N 38.21; found: C 16.15, H 1.88, N 37.96.

Preparation of [Cu(tz)]/[Cu(atz)] nanosheets (denoted as *p*-A_0H_{100}/*w*-$A_{100}H_0$, *p*/*w* for planar/wavy, A/H for amino/hydrogen). 15 mg of [Cu(tz)]/[Cu(atz)] microcrystalline dispersed in MeOH (40 mL) was treated by ultra-sonication (SXSONIC FS-300N, 300 W, 20 kHz) for 24 h under N_2 atmosphere, then left standing for 6 h. Finally, nanosheets in the upper part of the solution were collected by centrifugation (15000 r min^{-1}, 5 min).

Preparation of *p*-A_xH_{100-x} ($0<x\leq25$). Under N_2 atmosphere, ***p*-A_0H_{100}** (0.013 g, 0.1 mmol) was added into the MeOH solution of Hatz (6 mL, 0.17 and 0.33 mol L^{-1} for x = 12 and 25, respectively, higher concentration yielded amorphous product), then stirred vigorously for three days at 40 °C. Finally, the resulting suspension was collected by centrifugation (15000 r min^{-1}, 5 min). The x values were determined by ^{1}H-NMR, in which the samples were digested by 20% DCl in MeOH-D_4.

Preparation of *w*-A_xH_{100-x} (25≤*x*<100). Under N_2 atmosphere, ***w*-$A_{100}H_0$** (0.015 g, 0.1 mmol) was added into the MeOH solution of Htz (6 mL, 0.67 and 0.33 mol L^{-1} for x = 25 and 50, respectively, higher concentration yielded amorphous product), then stirred vigorously for three days at 40 °C. Finally, the resulting suspension was collected by centrifugation (15000 r min^{-1}, 5 min). The x values were determined by ^{1}H-NMR, in which the samples were digested by 20% DCl in MeOH-D_4.

X–ray absorption spectral measurement. The X-ray absorption experiments were carried out at the XAS station in Shanghai Synchrotron Radiation Facility (SSRF). The Cu K–edge XANES data was recorded in a transmission mode. The storage ring was operated at 3.5 GeV. Si (311) double–crystal was used as the monochromator.

Electrochemical measurements. 10 mg of the catalysts were dispersed in 1 mL of 7:2.5 (*v*/*v*) ethanol/water with Nafion (50 μL) by sonication to form a uniform suspension. 10 μL suspension was dropped on the glassy carbon electrode (GCE, surface area = 0.196 cm^2) and then dried in an N_2 atmosphere. The linear sweep voltammetry (LSV) was performed in a sealed H-type cell using a CHI760E electrochemical workstation at a scan rate of 10 mV s^{-1}. Each cell was injected into 0.1 M $KHCO_3$ electrolyte (15 mL), which was bubbled with Ar (20 mL min^{-1}) or CO_2 (20 mL min^{-1}) for at least 20 min. Ag/AgCl (3 M KCl) electrode and graphite electrode were used as the reference and counter electrode, respectively. All potentials were a calibrated with respect to reversible hydrogen electrode (RHE) using the conversion equation:

$$E\ (vs\ \text{RHE}) = E\ (vs.\ \text{Ag/AgCl}) + 0.197\ \text{V} + 0.0591 \times \text{pH} \qquad \text{(Equation 1)}$$

Product detection. The gas products were analyzed by an online Agilent 7890B gas chromatograph (GC) equipped with a thermal conductivity detector (TCD) detector (for H_2) and flame ionization detector (FID) detector (for CO, CH_4 and C_2H_4). The reactions were run for at least 240 s to remove the dead space in the electrolytic cell before gas products were collected for analysis. And the corresponding faradic efficiency was calculated as follows:

$$\text{FE}(\%) = zFC_iVP/jRT \times 100 \qquad \text{(Equation 2)}$$

z: the number of electrons required to form one molecule of product;

F: the Faraday constant (96485 C mol^{-1});

C_i: the concentration of the products;

V: the flow rate of CO_2 (20 mL min^{-1});

P: the pressure (1 atm);

j: the cell current (A) at a steady state;

R: Avogadro constant;

T: room temperature (K).

The electrochemical measurement for each catalyst was repeated for three samples synthesized in different batches, and three times (three electrodes) for each sample. The nine sets of data were used to calculate the average values and standard deviations.

The isotope-labeled experiments were performed using $^{13}CO_2$ under the same condition as those of $^{12}CO_2$, and the products were analyzed using an Agilent GC-mass spectrometry (7890B and 5977B) coupled with a GS CARBONPLOT capillary column. The liquid products of eCO_2RR were measured by using ^1H NMR spectroscopy with D_2O and DMSO as an internal standard.

Standard curves on GC. Four concentrations of standard mixed gases containing H_2, CO, CH_4 and C_2H_4 with CO_2 balance were used to set the standard curves for GC measurements. The concentration of the components (ppm) and the final standard curves are listed below.[S1]

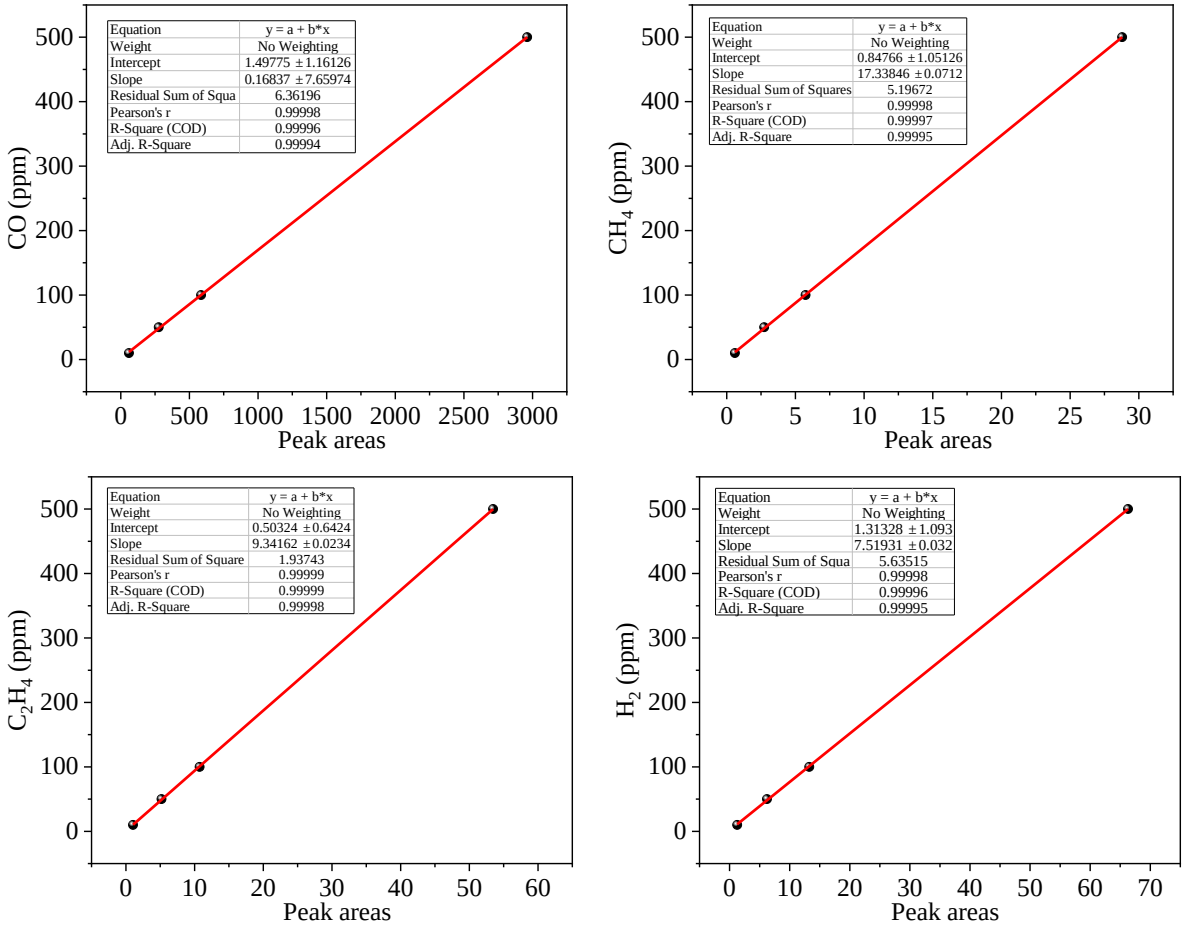

Computational simulations. All the calculations, including structure optimization and free energy calculations, were performed by periodic density functional theory (PDFT) using periodic structures as the model in the Materials Studio 5.5 package since these 2D structures are difficult to isolate a cluster. The structures of intermediates were optimized by the DMol^3 module. The generalized gradient approximation (GGA) with the Perdew–Burke–Ernzerhof (PBE) function was employed,[S2] as well as the Tkachenko–Scheffler (TS)[S3] vdW correction to accurately describe the long-range electrostatic interactions of CO_2RR species within catalysts.[S4,S5] Considering the solvation effect during CO_2 electroreduction, water was chosen as the solvent model (dielectric constant: 78.54). The convergence tolerance of energy, force and displacement convergence were set as 1×10^{-5} Ha, 2×10^{-3} Å and 5×10^{-3} Å, respectively. The core treatment was chosen as the effective core potential (ECP), and the electron treatment was performed by double numerical plus d-functions (DNP) basis set.

Single layers of [Cu(tz)] and [Cu(atz)] were used as the models for ***p*-A$_0$H$_{100}$** and ***w*-A$_{100}$H$_0$**, respectively, in which ***p*-A$_0$H$_{100}$** contains 32 atoms (4 molecular units) with unit-cell size of $10.6 \times 10.6 \times 10.8$ Å^3 and ***w*-A$_{100}$H$_0$** contains 40 atoms (4 molecular units) with unit-cell size of $10.4 \times 10.6 \times 14.0$ Å^3.[S6,S7] The models of ***p*-A$_x$H$_{100-x}$** were built from the ***p*-A$_0$H$_{100}$** model by replacing a certain amount of tz^- with atz^-, and those of ***w*-A$_x$H$_{100-x}$** were from the ***w*-A$_{100}$H$_0$** model by replacing a certain amount of atz^- with tz^- (Figs. S25–S30). For example, for ***p*-A$_{25}$H$_{75}$**, we replaced one hydrogen atom on tz^- with one amino group in ***p*-A$_0$H$_{100}$**; for ***w*-A$_{25}$H$_{75}$**, one amino group on atz^- was replaced by one hydrogen atom in ***w*-A$_{100}$H$_0$**, because there are four triazoles in the unit-cell and these four triazolates are equivalent, replacing one is 25%, then the structure was optimized by PDFT. Furthermore, for ***p*-A$_{31.2}$H$_{68.8}$/*w*-A$_{12.5}$H$_{87.5}$**, a 2×2 supercell of ***p*-A$_{25}$H$_{75}$/*w*-A$_{25}$H$_{75}$** were employed, and ***p*-A$_{31.2}$H$_{68.8}$** could be obtained by replacing one of the hydrogen atoms with an amino group in the supercell of ***p*-A$_{25}$H$_{75}$** or vice versa for ***w*-A$_{12.5}$H$_{87.5}$**. For ***w*-A$_0$H$_{100}$**, all of the amino groups in ***w*-A$_0$H$_{100}$** were replace by hydrogen atoms, then the structure was optimized by PDFT with partial restriction. The Gibbs free energy (ΔG) of the intermediates in possible catalytic pathways for hydrogen (H_2), and ethylene (C_2H_4) were calculated, which were estimated using the following equation:

$$\Delta G = \Delta E + \Delta E_{ZPE} - T\Delta S \qquad \text{(Equation 3)}$$

Where ΔE is the reaction energy; ΔE_{ZPE} is the difference in the zero-point energy, and ΔS is the change in entropy of reactants and products. T is the temperature which was set to 298.15 K. Here, ΔE_{ZPE} and ΔS were calculated from the vibration energy of the intermediates and the gas phase adsorbates.

The preferred sorption locations of H_2O or CO_2 were searched through grand canonical Monte Carlo (GCMC) simulations by using the fixed loading task and Metropolis method in the sorption calculation

module. The host framework and the gas molecule were both regarded as rigid. The simulation box consisted of one unit cell. For all the GCMC simulations, all the frameworks and the gas molecules were described by the universal forcefield. The Mulliken charges calculated by PDFT, were employed to the framework atoms and guest atoms, respectively. The cutoff distance was set to 12.5 Å for the Lennard-Jones (LJ) interactions, and the electrostatic interactions and the van der Waals interactions were handled using the Ewald and Atom based summation method, respectively. The loading steps, equilibration steps and the production steps were all set to 1.0×10^7. The binding energy $\Delta E = E_{\text{host + guest}} - E_{\text{host}} - E_{\text{guest}}$, where $E_{\text{host + guest}}$ and E_{host} (E_{guest}) are the energies of the host-guest system and the isolated host (guest), respectively.

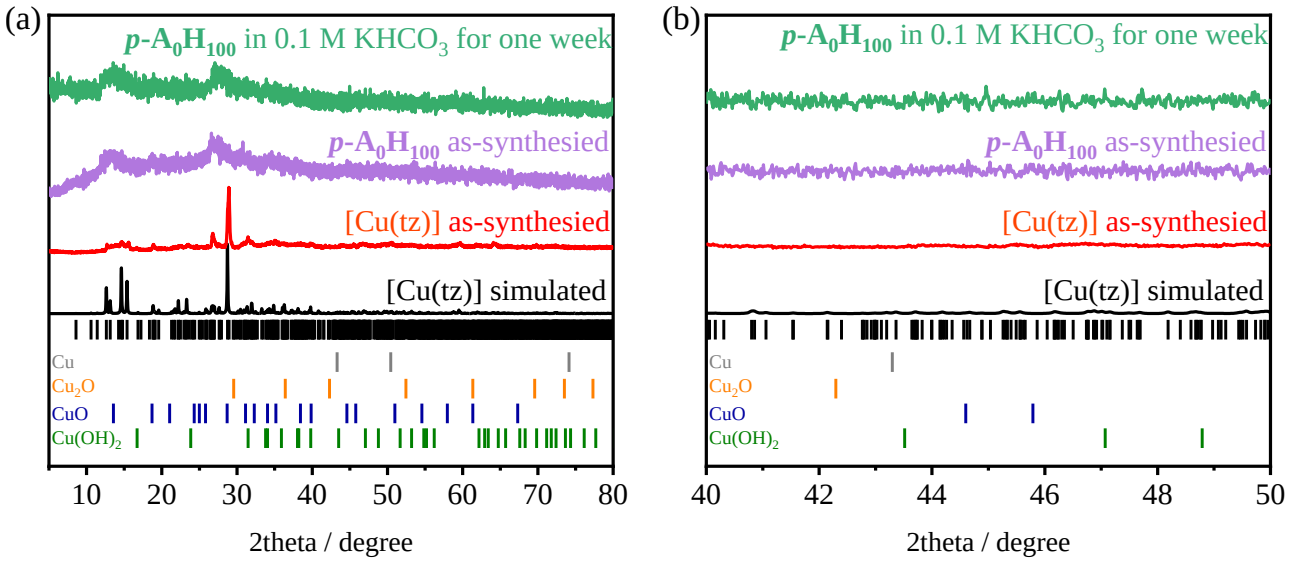

Fig. S1 PXRD patterns of [Cu(tz)] and ***p*-A$_0$H$_{100}$**. (a) Whole range. (b) Enlarged part.

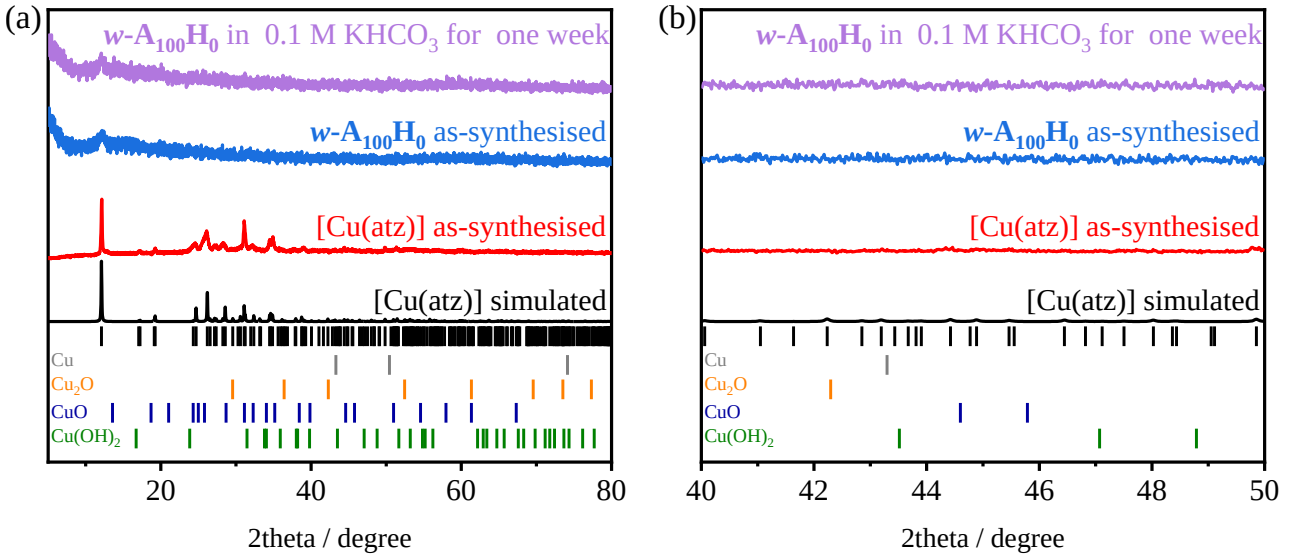

Fig. S2 PXRD patterns of [Cu(atz)] and ***w*-A$_{100}$H$_0$**. (a) Whole range. (b) Enlarged part.

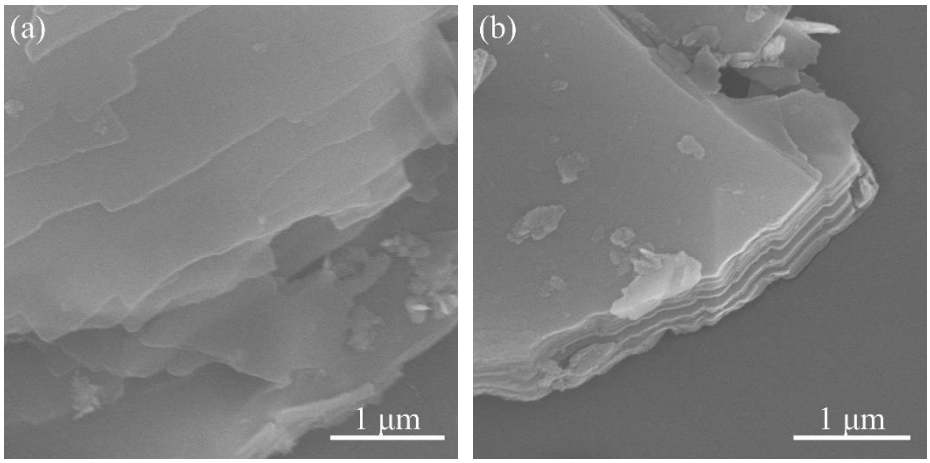

Fig. S3 SEM images of (a) [Cu(tz)] and (b) [Cu(atz)].

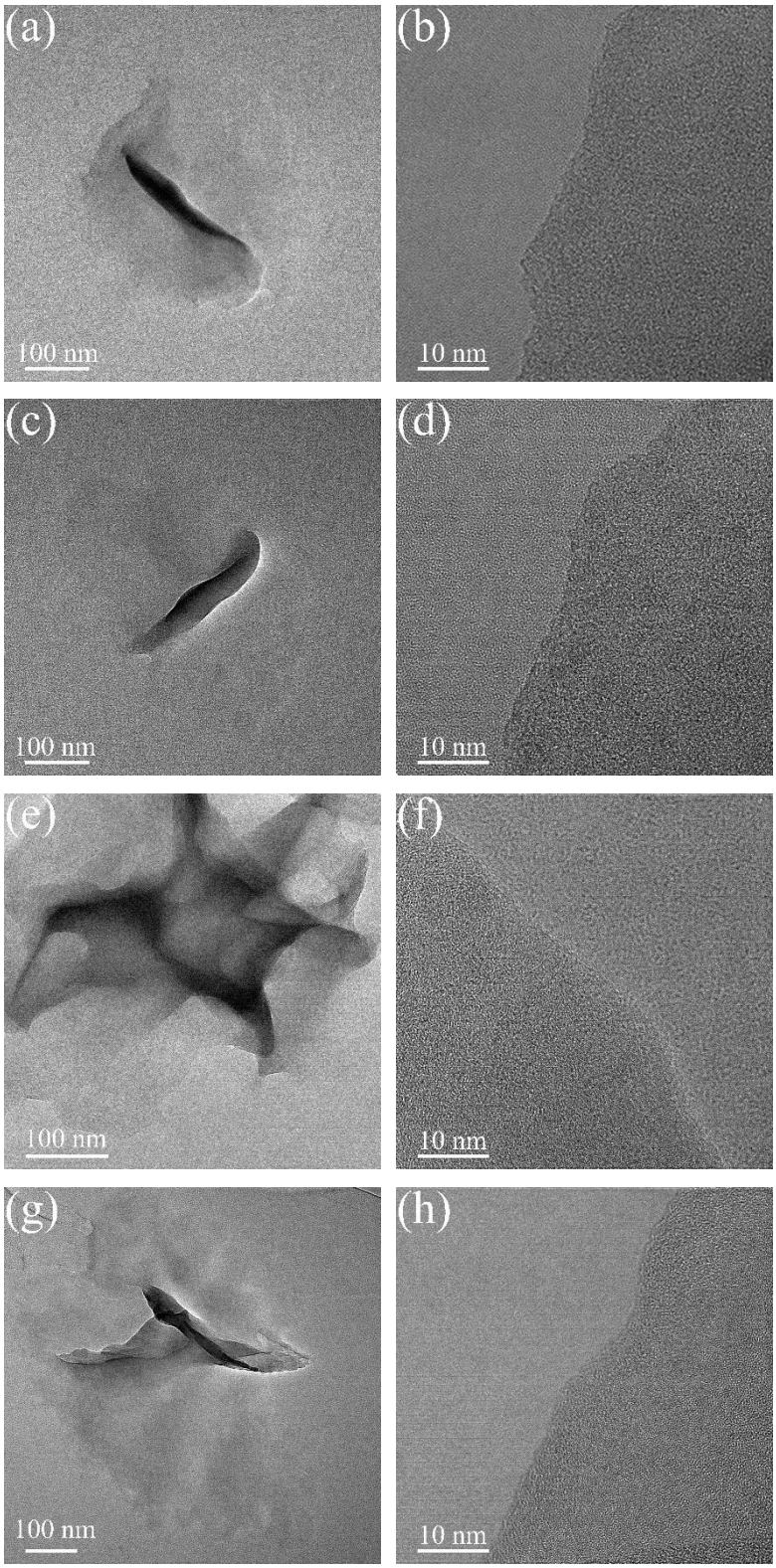

Fig. S4 (a,c,e,g) TEM and (b,d,f,h) HRTEM images. (a–d) ***p*-A_0H_{100}** and (e–h) ***w*-$A_{100}H_0$**. (a,b,e,f) Before and (c,d,g,h) after CO_2RR.

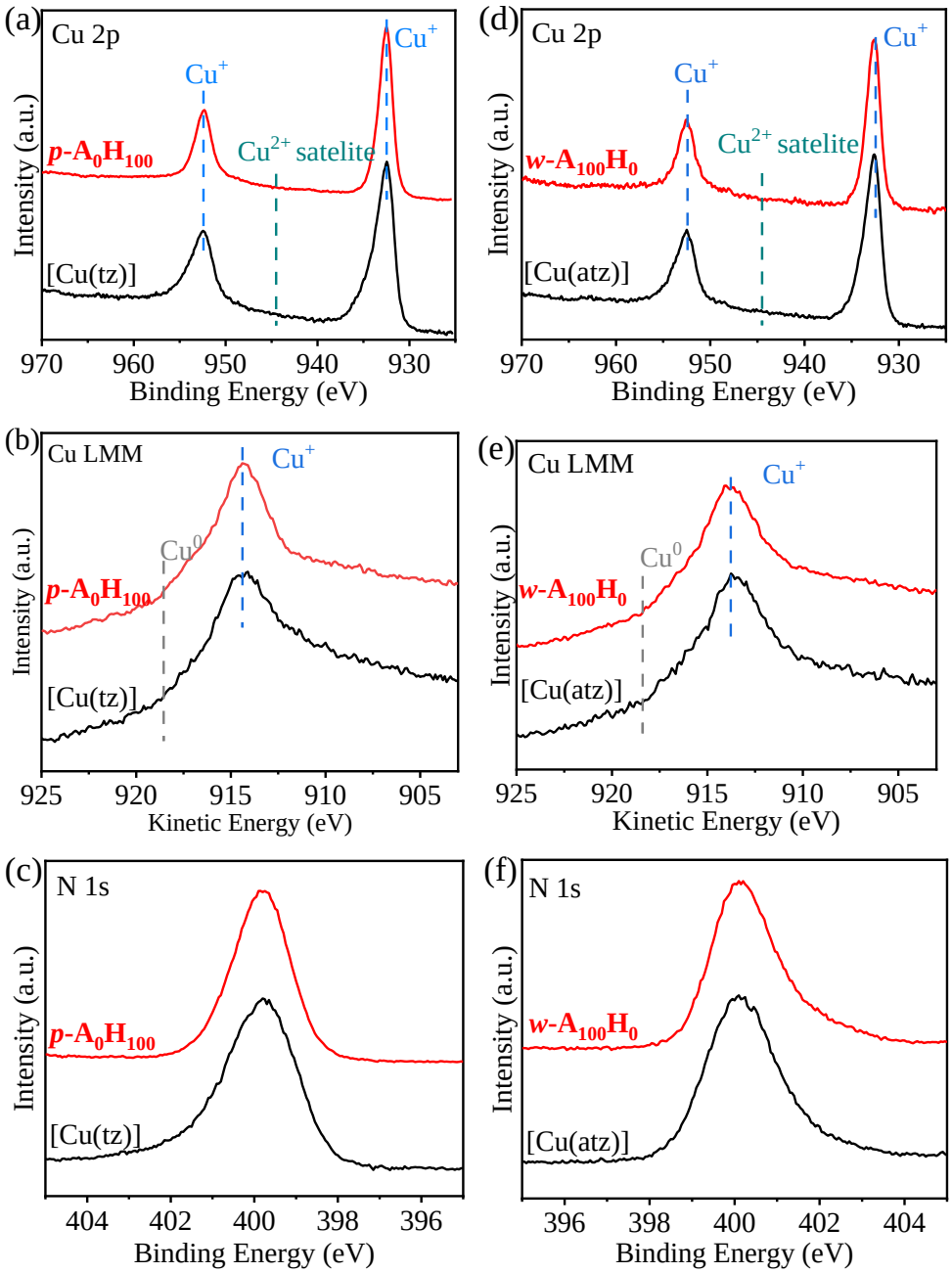

Fig. S5 XPS spectra of (a–c) [Cu(tz)]/***p*-A$_0$H$_{100}$** and (d–e) [Cu(atz)]/***w*-A$_{100}$H$_0$**. (a,d) Cu 2p region. (b,e) Cu LMM region. (c,f) N 1s region.

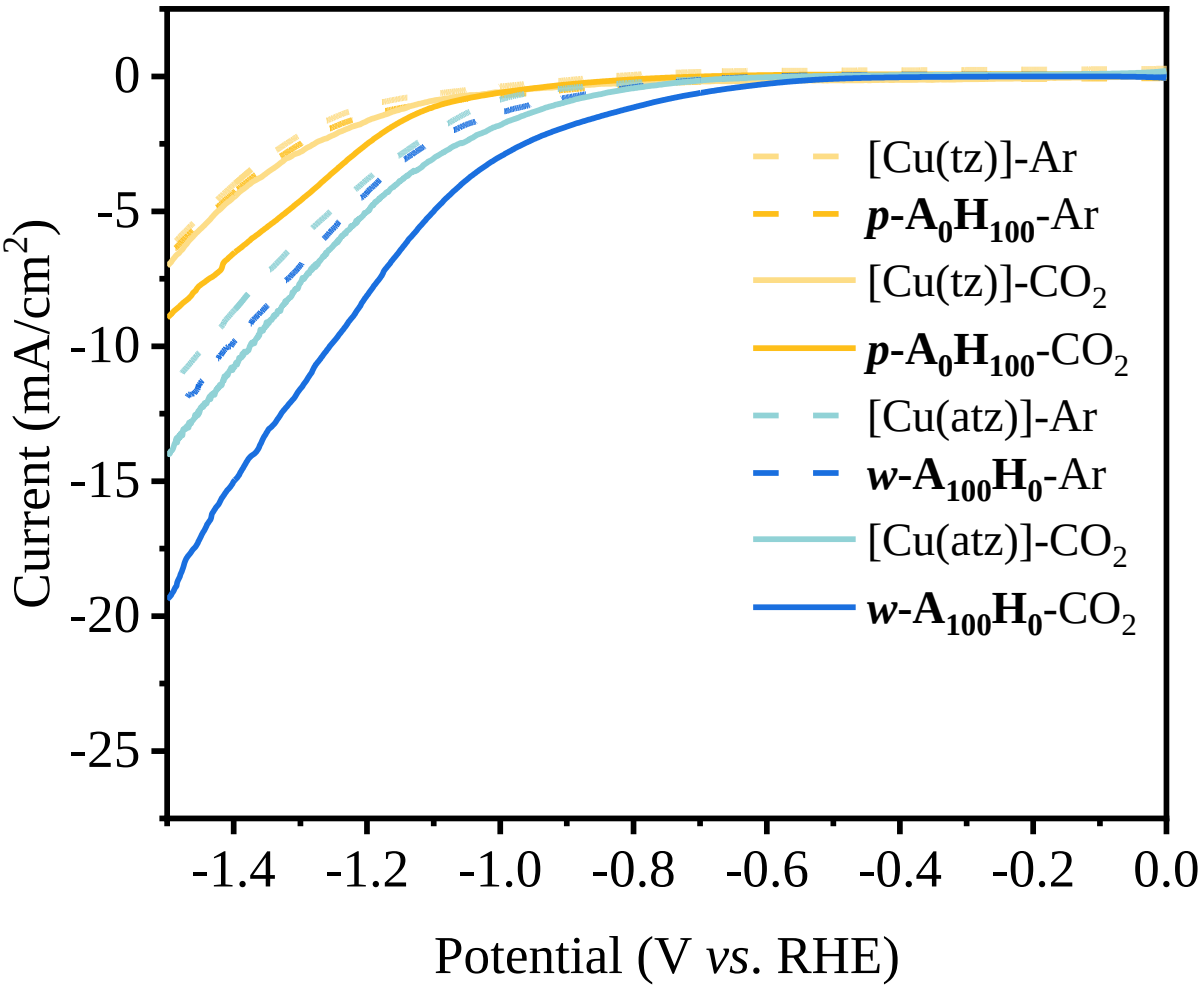

Fig. S6 LSV curves for [Cu(tz)], [Cu(atz)], ***p*-A$_0$H$_{100}$** and ***w*-A$_{100}$H$_0$**.

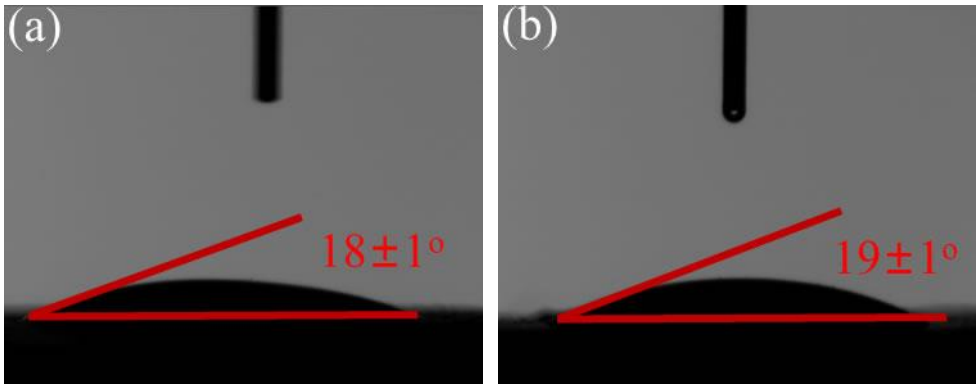

Fig. S7 Typical photographs for water contact angle tests for (a) ***p*-A$_0$H$_{100}$** and (b) ***w*-A$_{100}$H$_0$**.

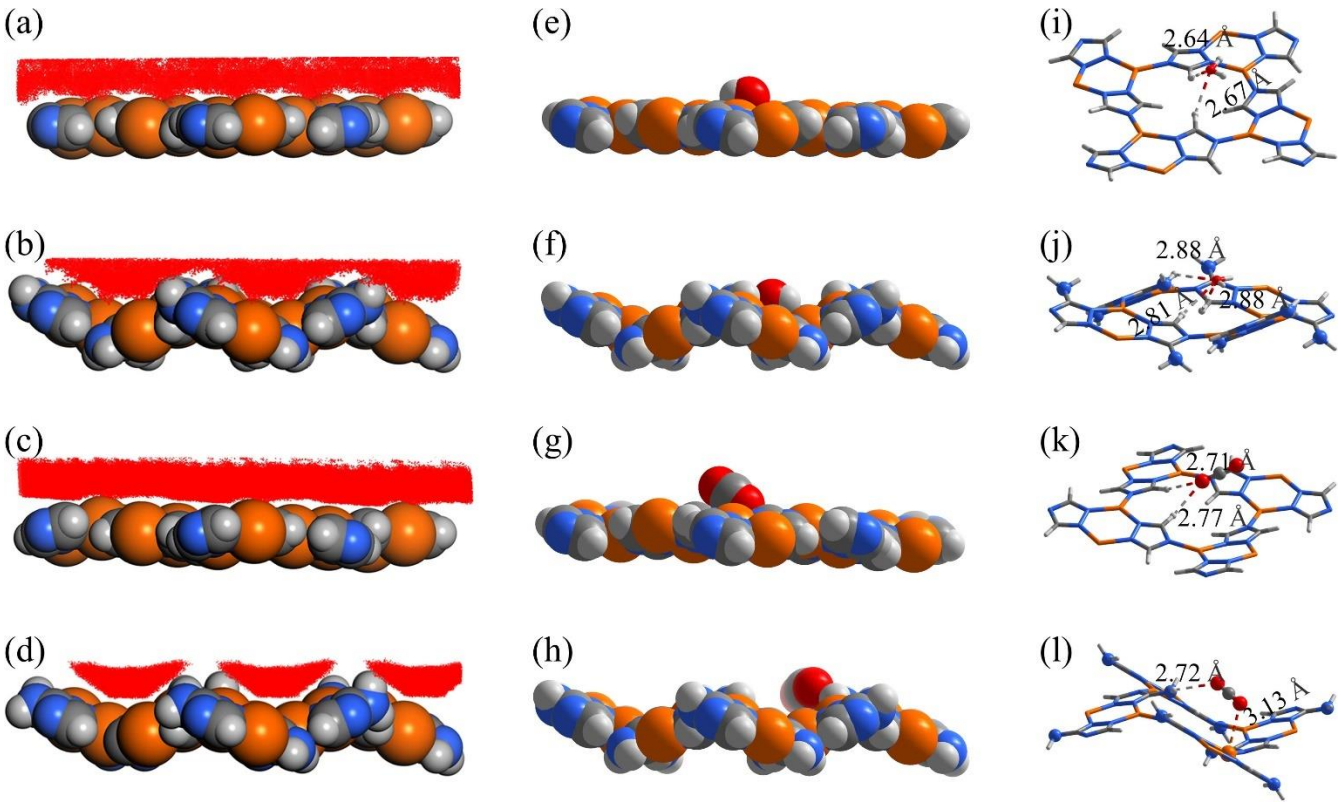

Fig. S8 (a-h) GCMC simulated adsorption structures for H_2O/CO_2 on ***p*-A$_0$H$_{100}$** and ***w*-A$_{100}$H$_0$**. (a–d) The density fields of the preferred locations of H_2O (a,b) and CO_2 (c,d) on ***p*-A$_0$H$_{100}$** (a,c) and ***w*-A$_{100}$H$_0$** (b,d). (e–h) The preferred adsorption structures for H_2O (e,f) and CO_2 (g,h) on ***p*-A$_0$H$_{100}$** (e,g) and ***w*-A$_{100}$H$_0$** (f,h) viewed perpendicularly to the coordination layers. (i–l) PDFT-optimized preferred adsorption structures for H_2O (i,j) and CO_2 (k,l) on ***p*-A$_0$H$_{100}$** (i,k) and ***w*-A$_{100}$H$_0$** (j,l).

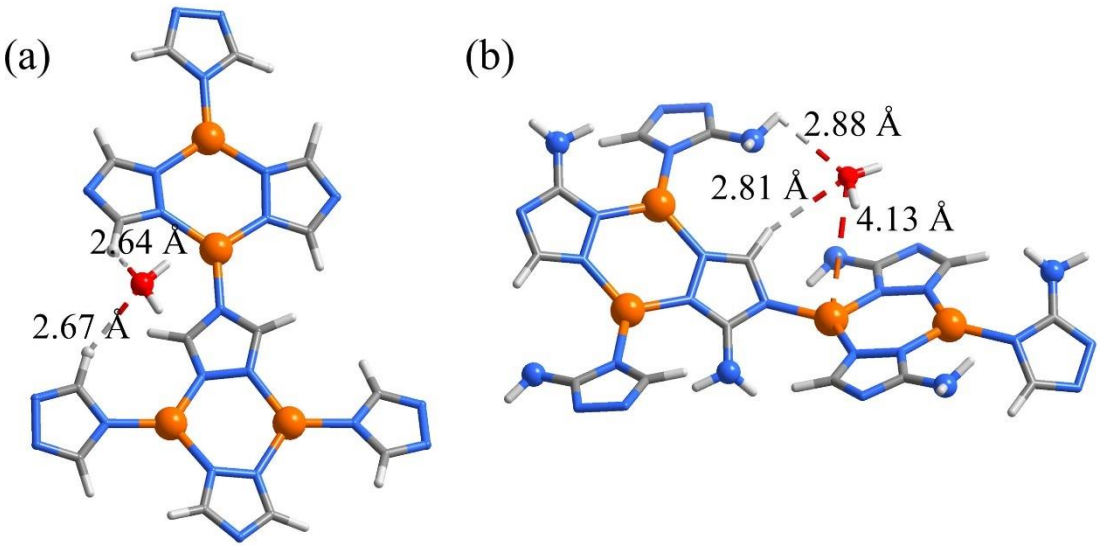

Fig. S9 Interactions between H_2O and (a) ***p*-A_0H_{100}** and (b) ***w*-$A_{100}H_0$**.

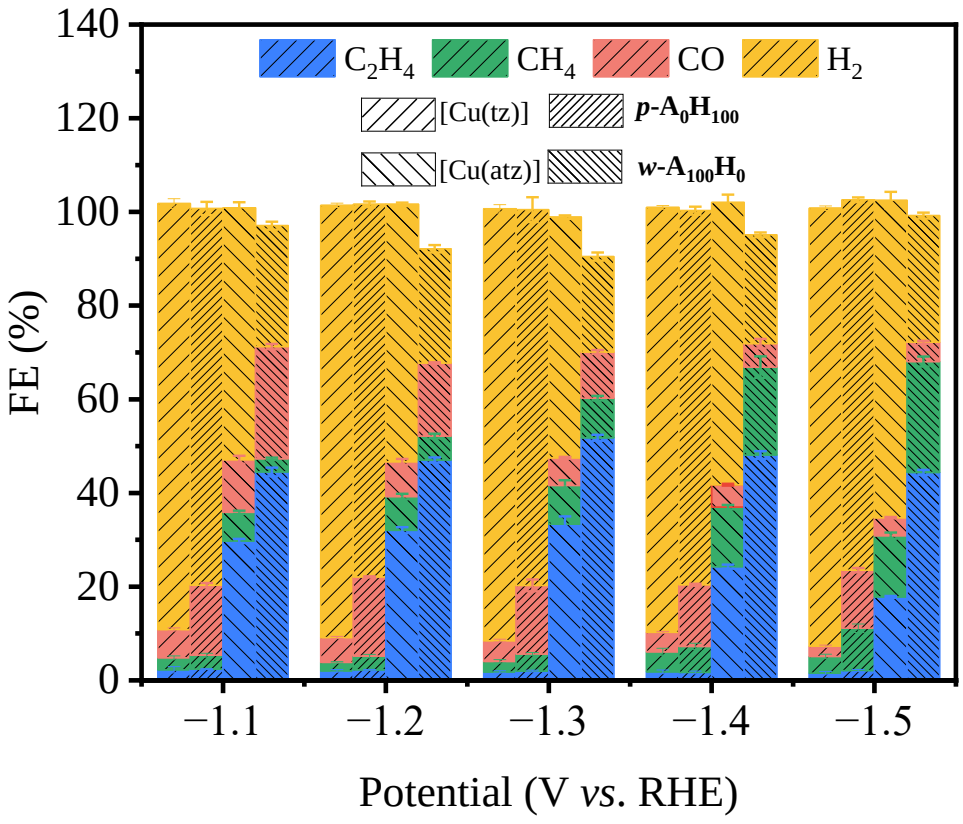

Fig. S10 Potential dependent FE of gas products for [Cu(tz)], [Cu(atz)], ***p*-A_0H_{100}** and ***w*-$A_{100}H_0$**. Obviously, the exfoliated nanosheets exhibited much higher CO_2RR performances.

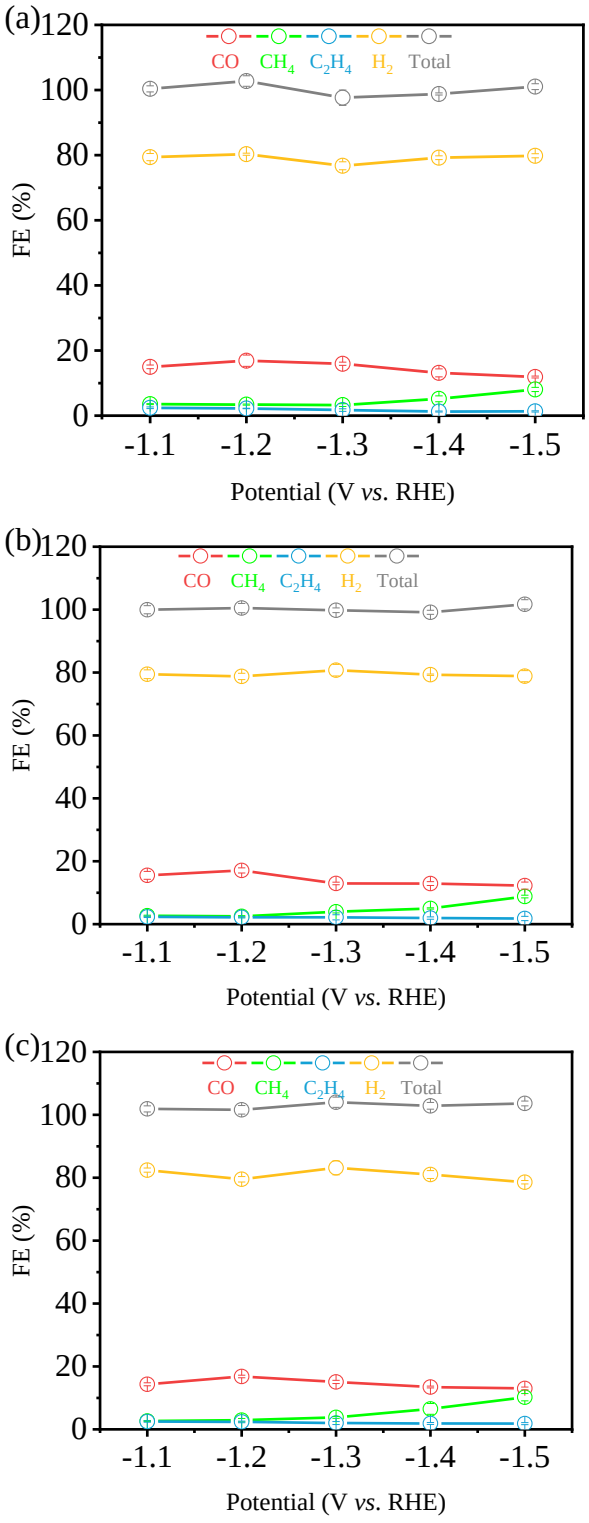

Fig. S11 Potential dependent FE of gas products for ***p*-A$_0$H$_{100}$** samples synthesized in three batches. (a) First, (b) Second, (c) Third batch.

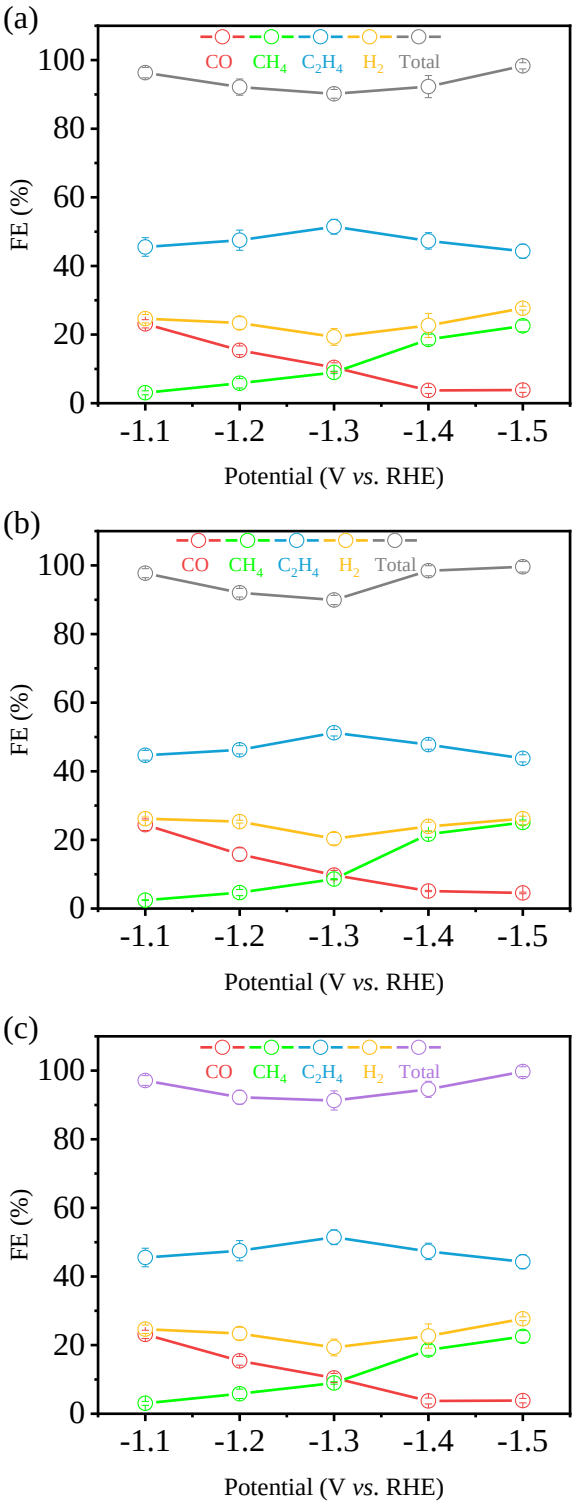

Fig. S12 Potential dependent FE of gas products for the ***w*-A$_{100}$H$_0$** samples synthesized in three batches. (a) First, (b) Second, (c) Third batch.

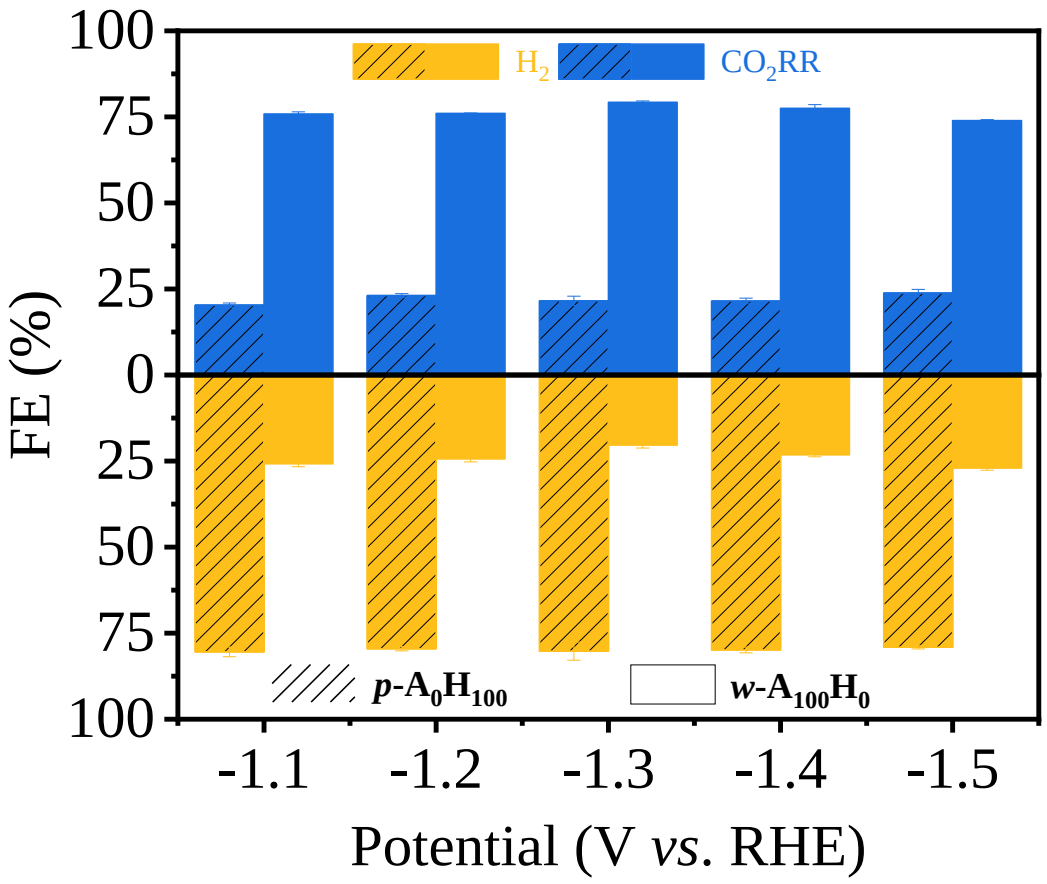

Fig. S13 Potential dependent FE of gas products for ***p*-A_0H_{100}** and ***w*-$A_{100}H_0$**.

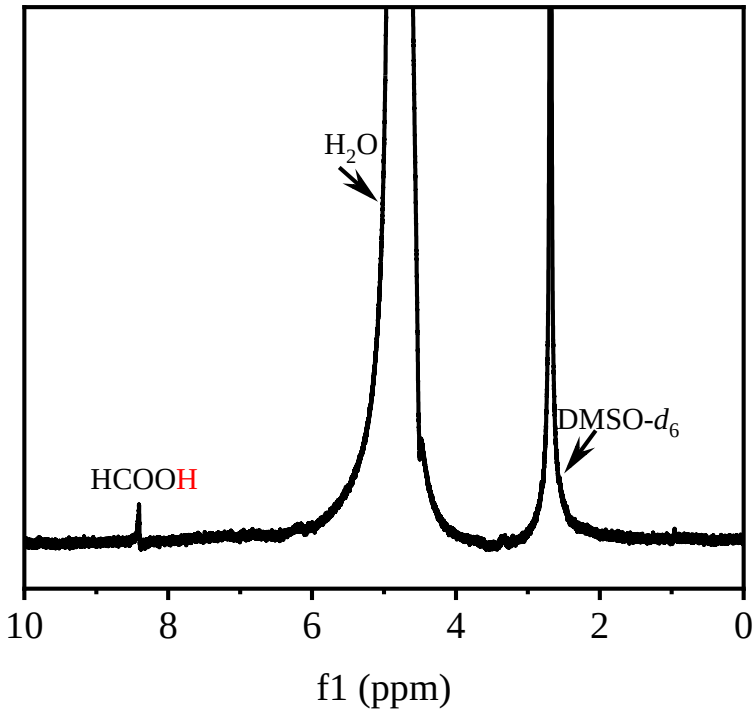

Fig. S14 Representative ^{1}H NMR spectrum of the electrolyte after CO_2RR.

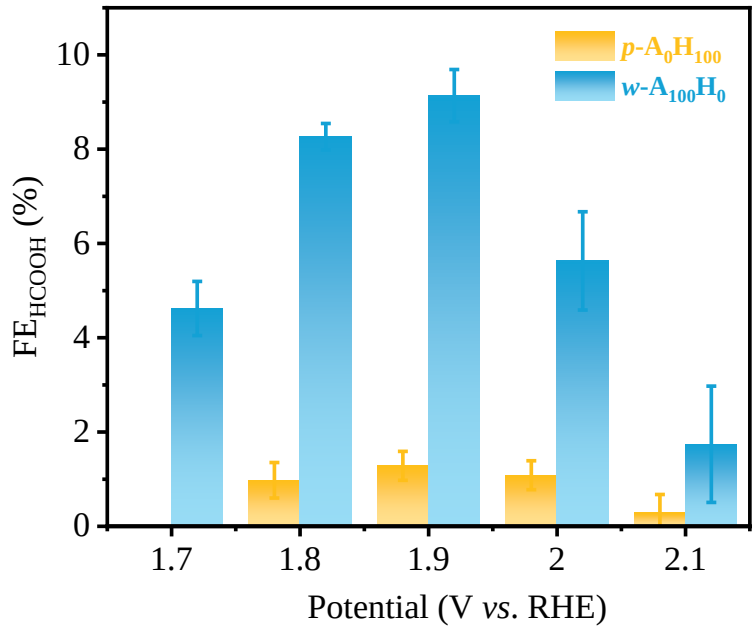

Fig. S15 Potential dependent FE of liquid products for ***p*-A$_0$H$_{100}$** and ***w*-A$_{100}$H$_0$**.

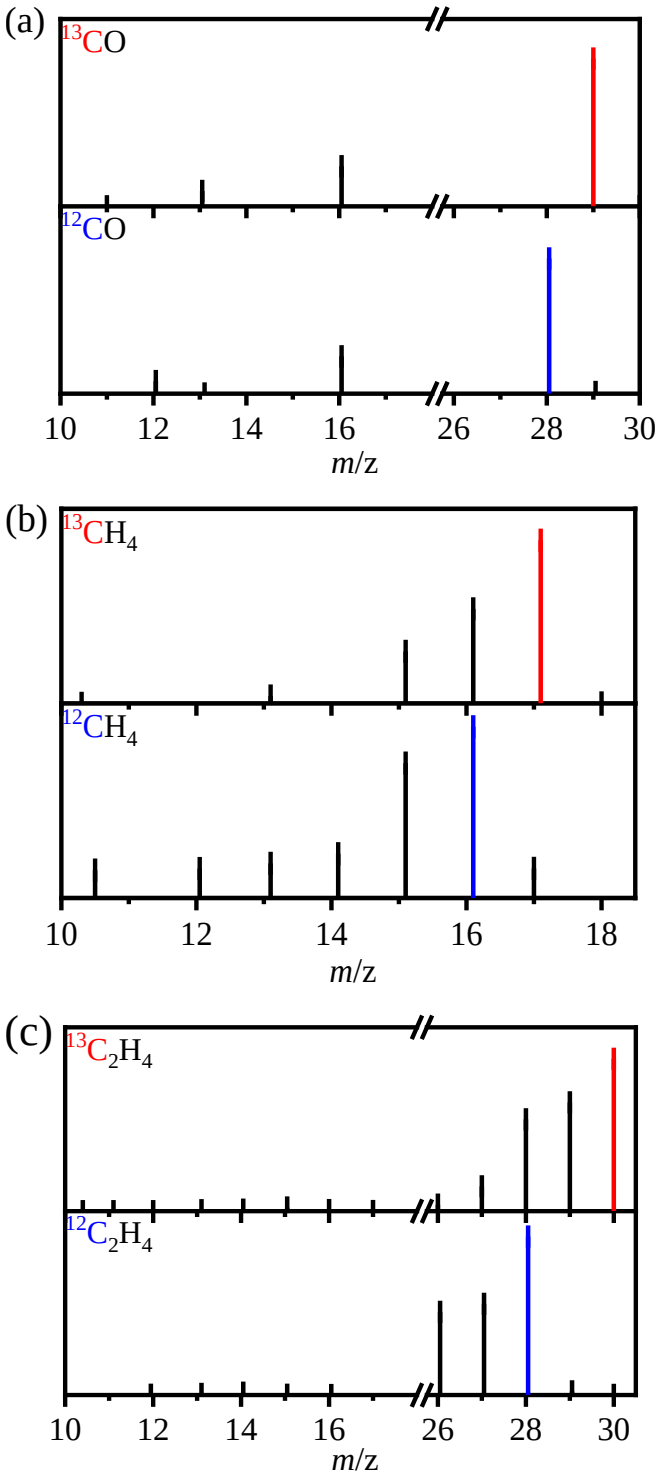

Fig. S16 Mass spectra extracted from GC-MS analysis of (a) CO, (b) CH_4 and (c) C_2H_4 produced from CO_2RR using $^{12}CO_2$ and $^{13}CO_2$.

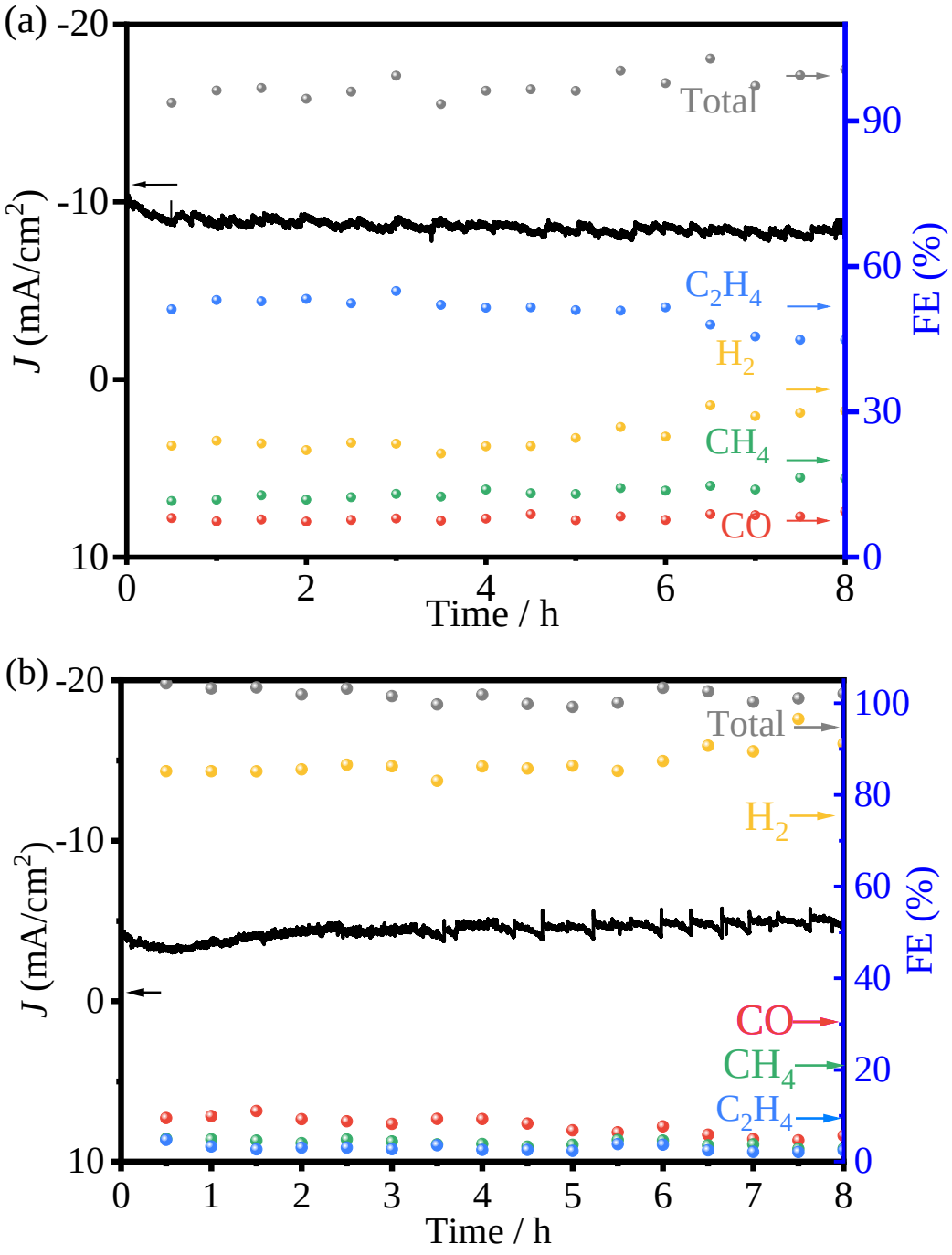

Fig. S17 Chronoamperometry of (a) ***w*-A$_{100}$H$_0$** and (b) ***p*-A$_0$H$_{100}$** at −1.3 V.

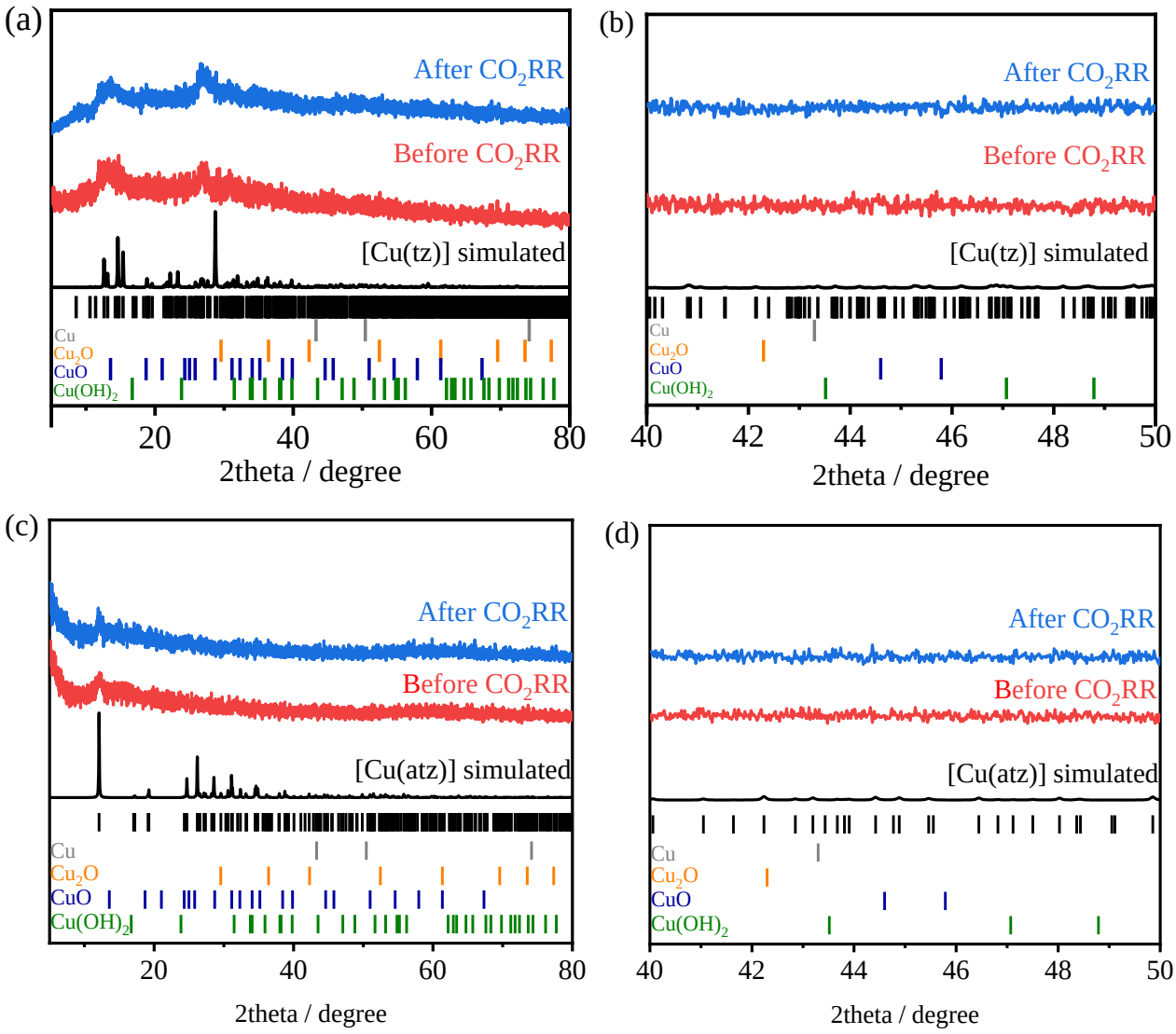

Fig. S18 PXRD patterns of (a,b) ***p*-A_0H_{100}** and (c,d) ***w*-$A_{100}H_0$** before and after CO_2RR. (a,c) Whole range. (b,d) Enlarged part.

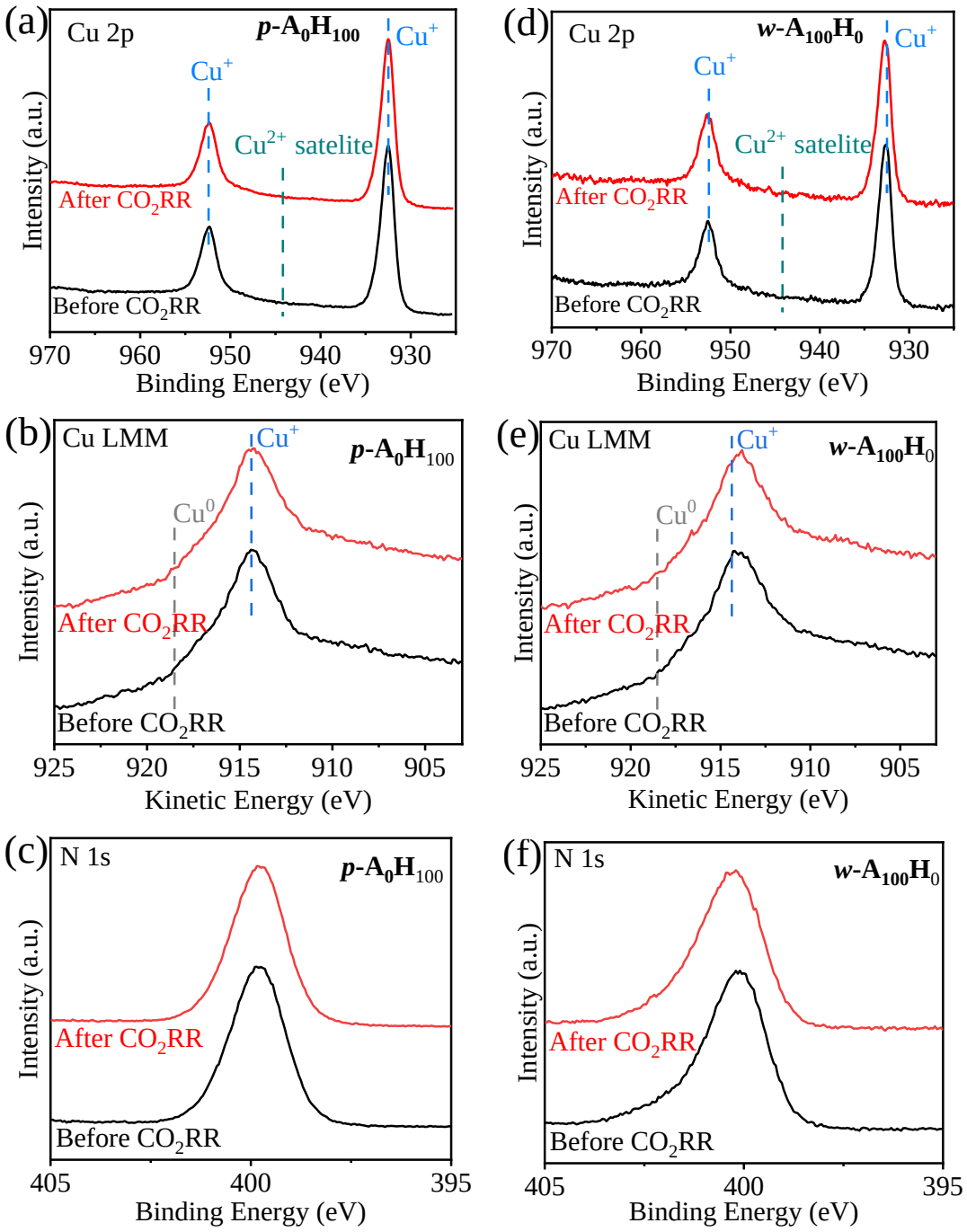

Fig. S19. XPS spectra of (a–c) ***p*-A$_0$H$_{100}$**, and (d–e) ***w*-A$_{100}$H$_0$** before and after CO_2RR. (a,d) Cu 2p region. (b,e) Cu LMM region. (c,f) N 1s region.

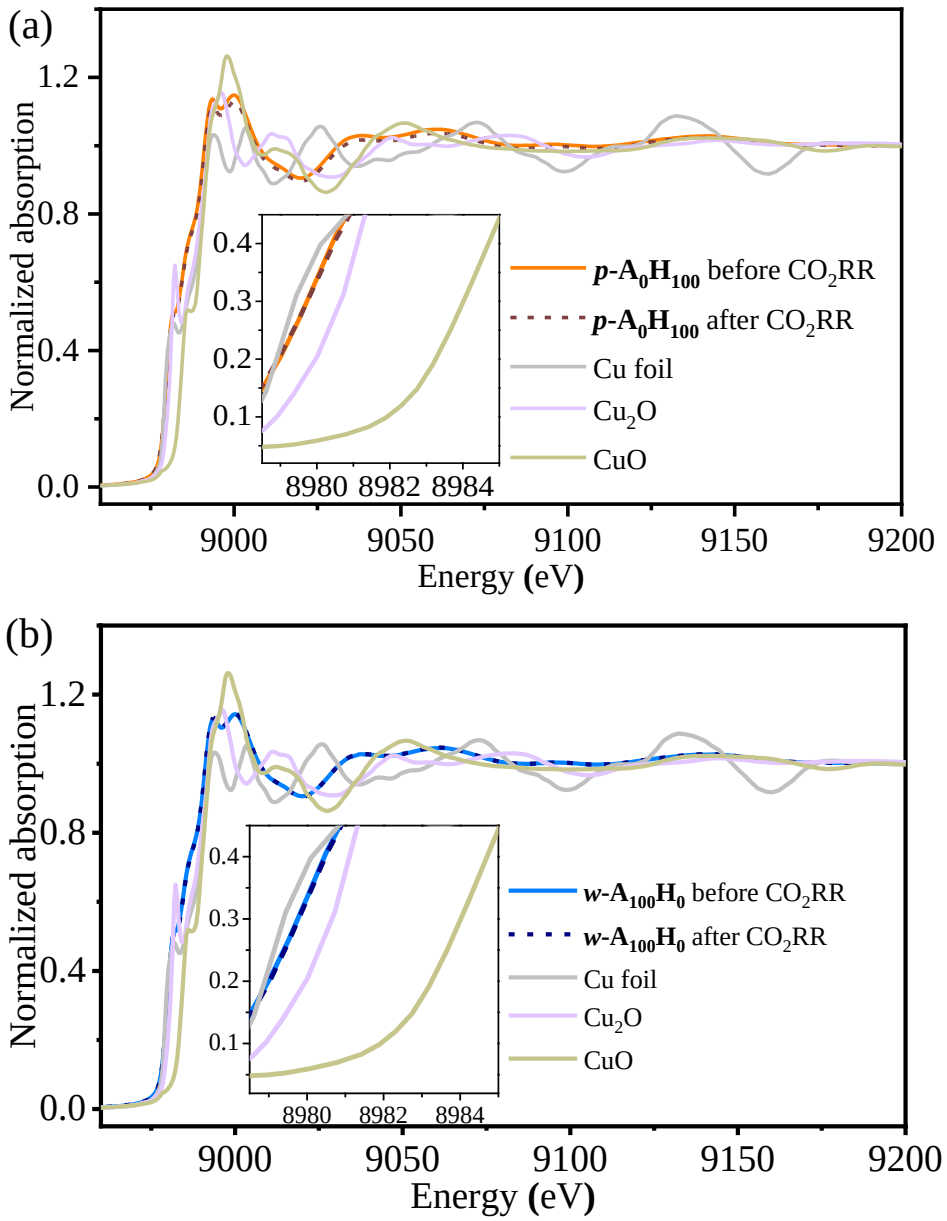

Fig. S20 Cu K-edge XANES spectra of (a) ***p*-A_0H_{100}** and (b) ***w*-$A_{100}H_0$** before and after CO_2RR.

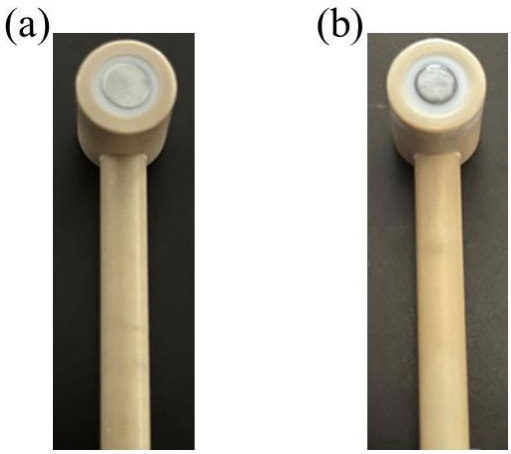

Fig. S21 The photograph of electrode (a) before and (b) after CO_2RR.

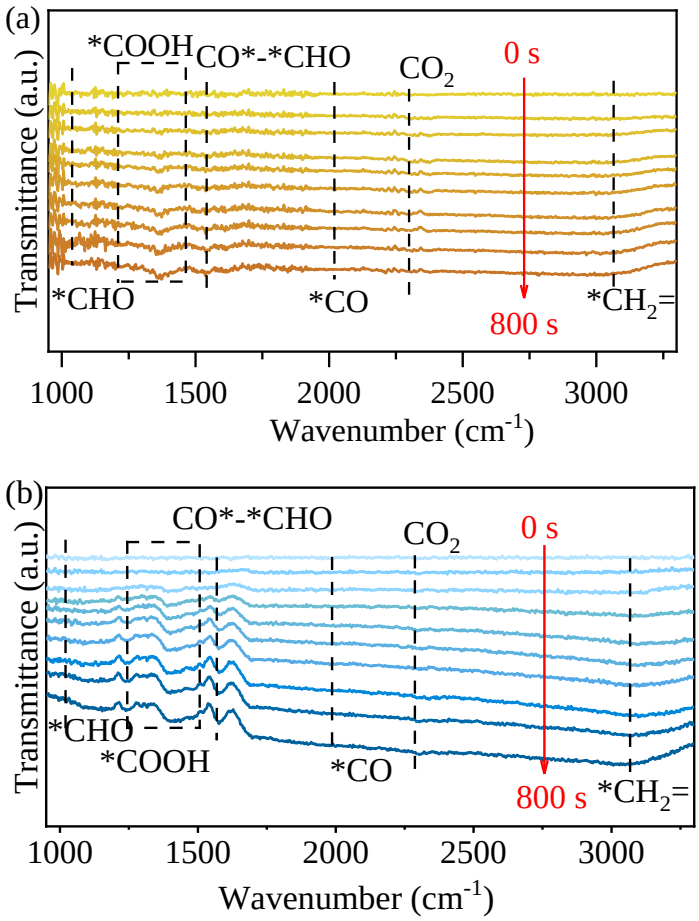

Fig. S22 *Operando* ATR−FTIR spectra of (a) ***p*-A_0H_{100}** and (b) ***w*-$A_{100}H_0$** at –1.3 V.

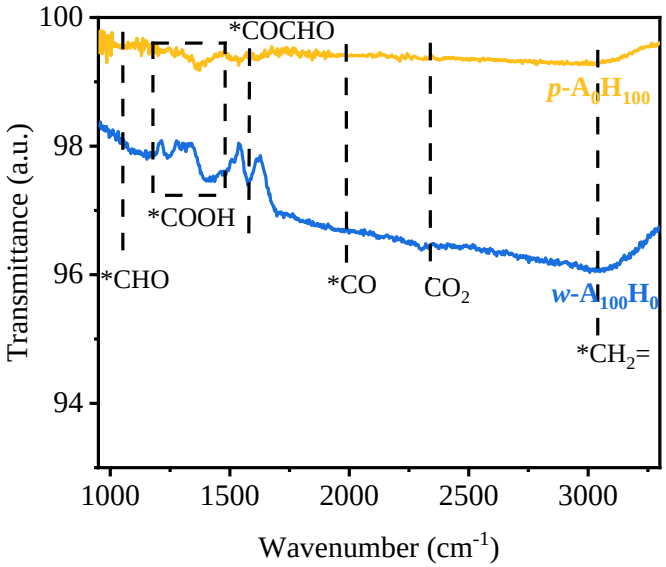

Fig. S23 *Operando* ATR−FTIR spectra of (a) ***p*-A$_0$H$_{100}$** and (b) ***w*-A$_{100}$H$_0$** at –1.3 V for 800 s.

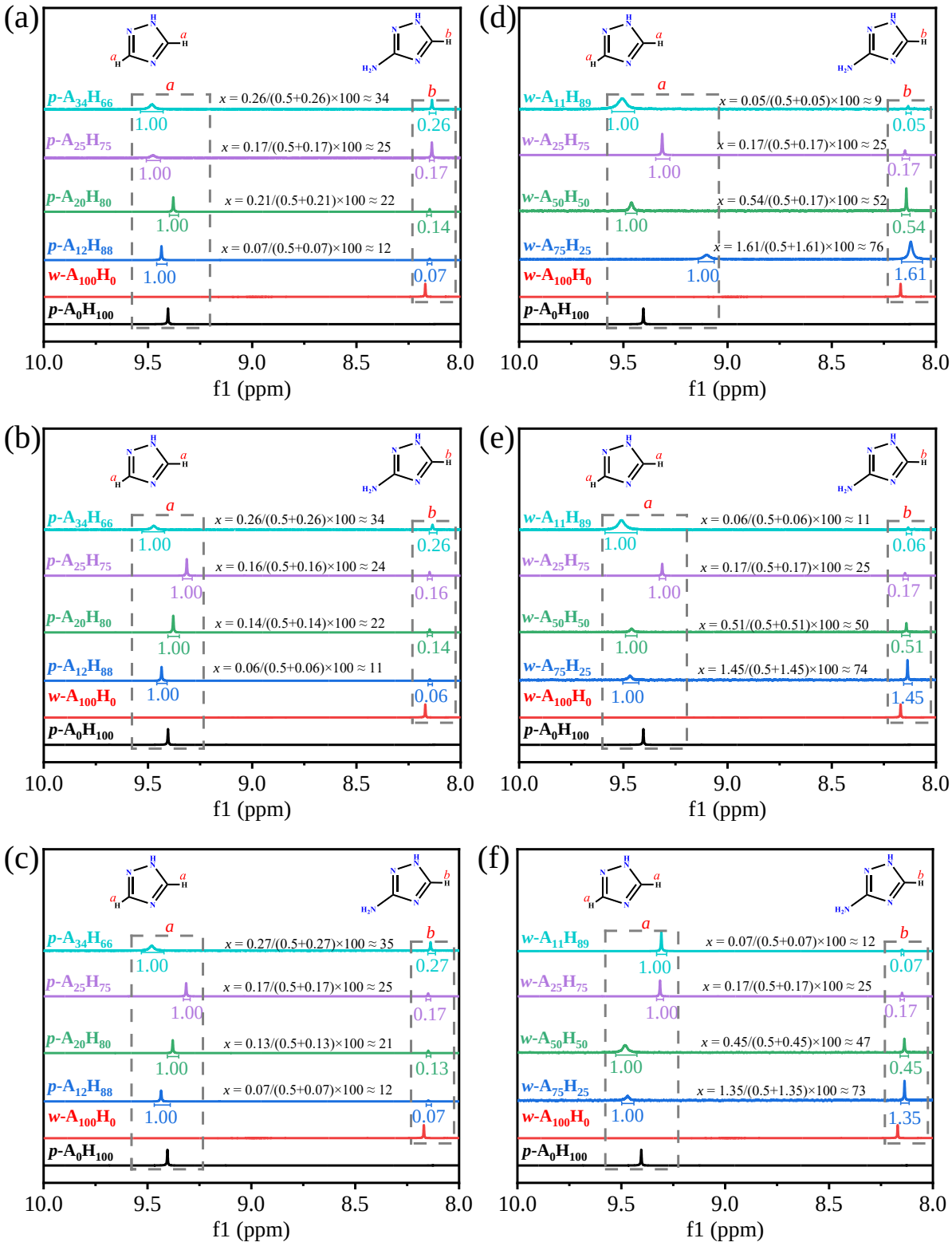

Fig. S24 ^{1}H-NMR spectra of the acid-digested (a-c) ***p*-A$_x$H$_{100-x}$** and (d-f) ***w*-A$_x$H$_{100-x}$** samples synthesized in three batches (the peaks shifted due to acidification of samples). (a,d) First, (b,e) Second, (c,f) Third batch.

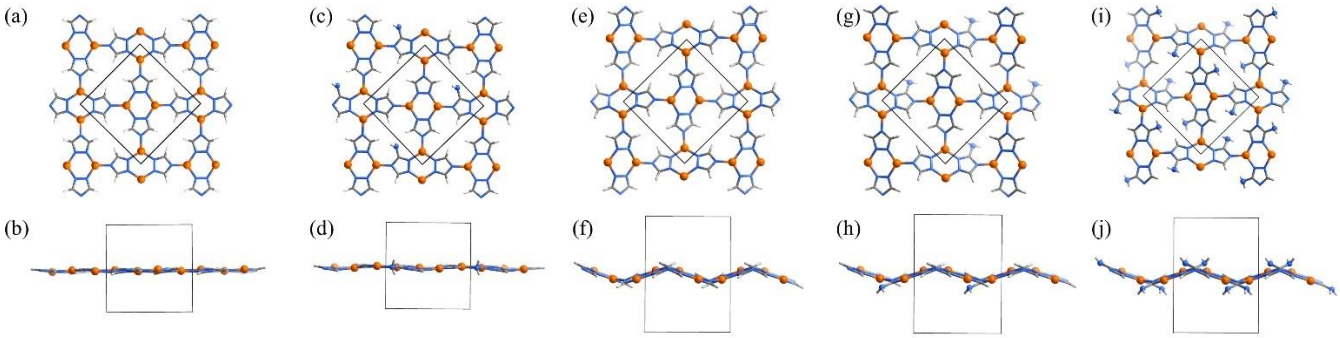

Fig. S25 The model structures of (a,b) ***p*-A$_0$H$_{100}$**, (c,d) ***p*-A$_{25}$H$_{75}$**, (e,f) ***w*-A$_0$H$_{100}$**, (g,h) ***w*-A$_{25}$H$_{75}$** and (i,j) ***w*-A$_{100}$H$_0$** for computational calculations at the perspective view perpendicular (a,c,e,g,i) and along (b,d,f,h,j) to the layers.

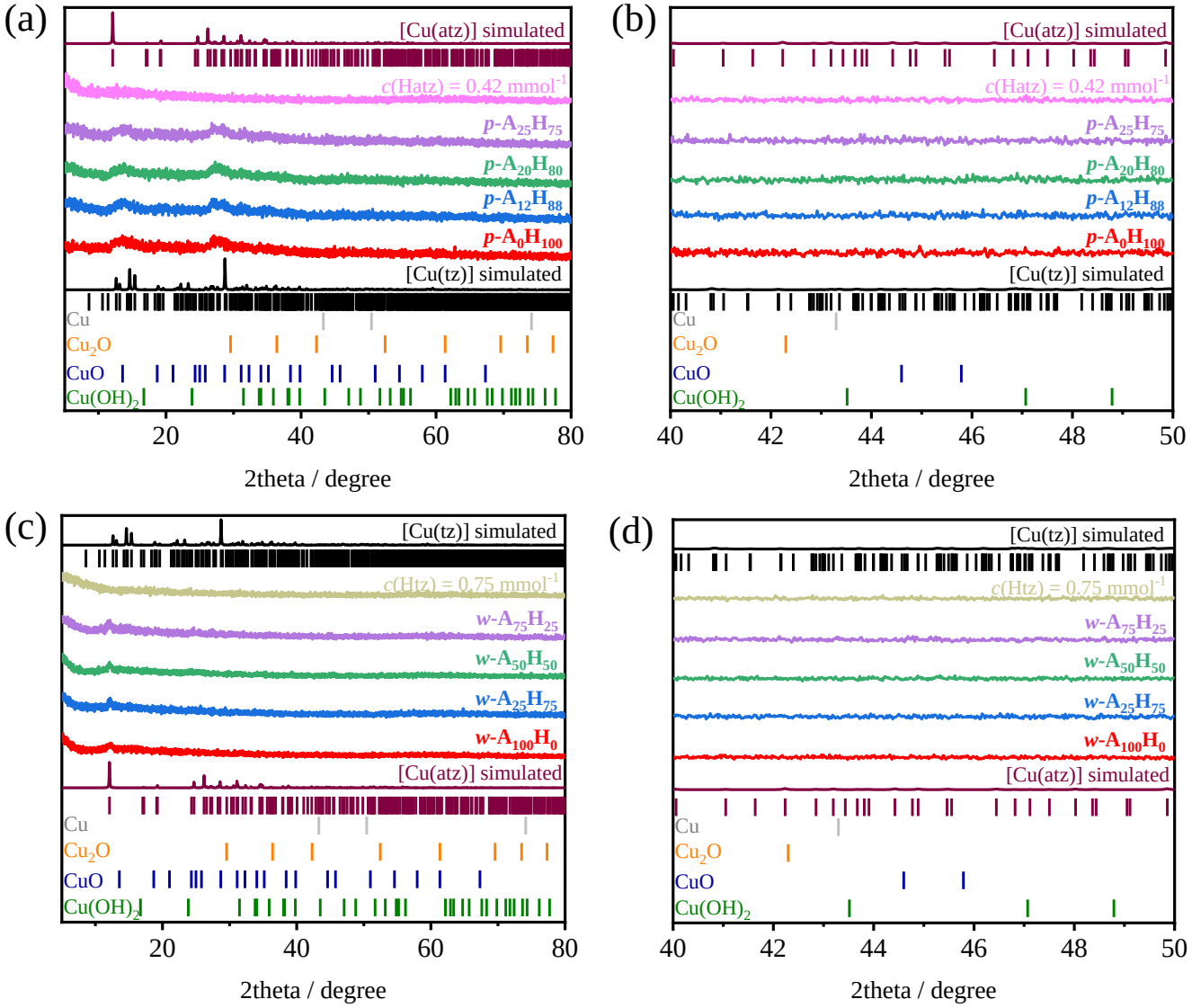

Fig. S26 PXRD patterns of (a,b) ***p*-A$_x$H$_{100-x}$**, (c,d) ***w*-A$_x$H$_{100-x}$**. (a,c) Whole range. (b,d) Enlarged part.

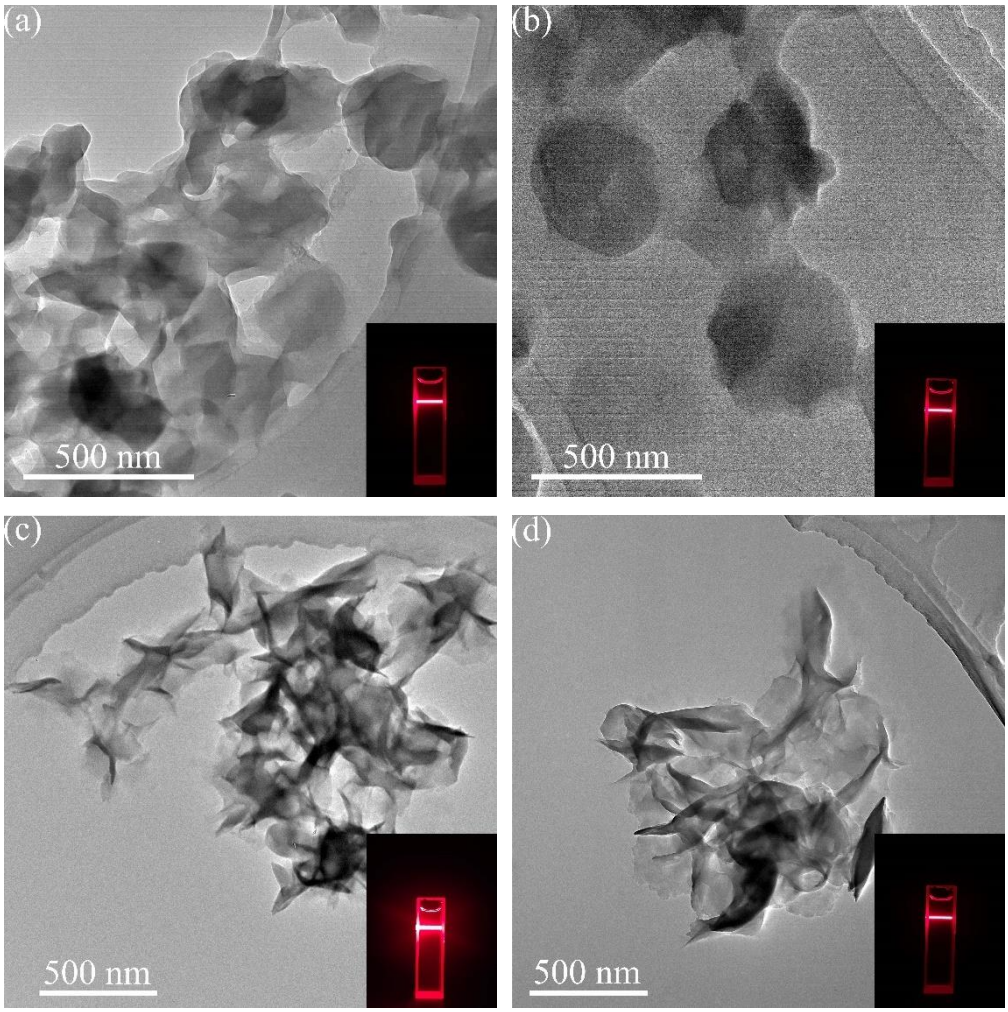

Fig. S27 TEM images of (a) ***p*-$A_{12}H_{88}$**, (b) ***p*-$A_{25}H_{75}$**, (c) ***w*-$A_{25}H_{75}$**, and (d) ***w*-$A_{50}H_{50}$**.

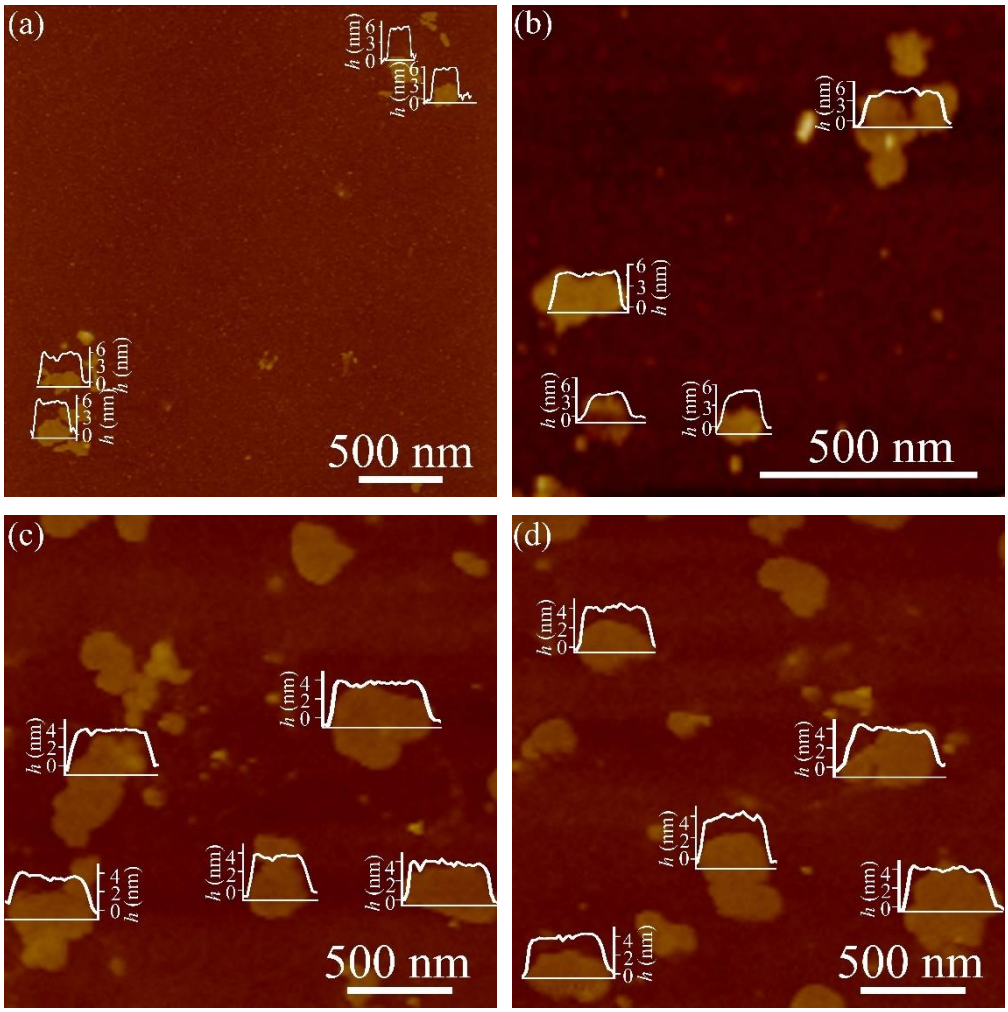

Fig. S28 AFM images of (a) ***p*-$A_{12}H_{88}$**, (b) ***p*-$A_{25}H_{75}$**, (c) ***w*-$A_{25}H_{75}$**, and (d) ***w*-$A_{50}H_{50}$**.

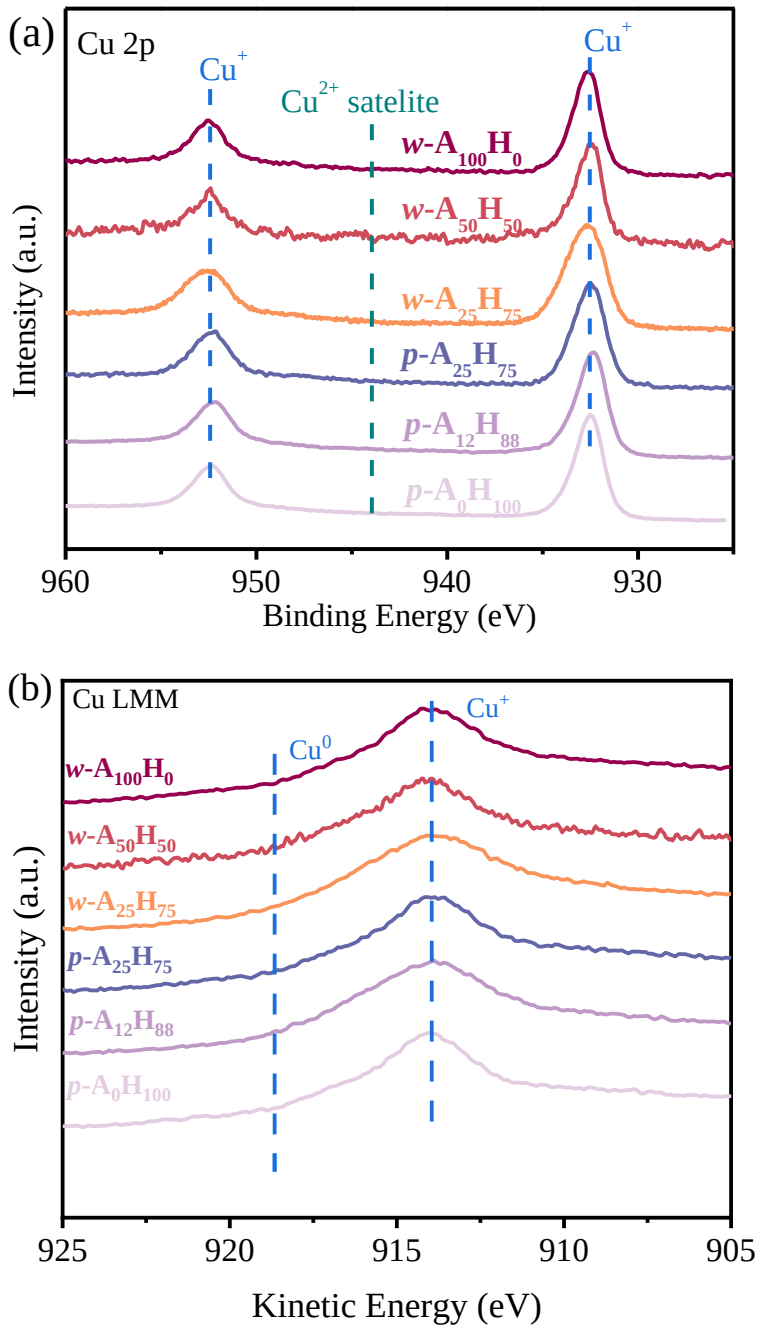

Fig. S29 XPS spectra of ***p*-A$_x$H$_{100-x}$** and ***w*-A$_x$H$_{100-x}$**. (a) Cu 2p region. (b) Cu LMM region.

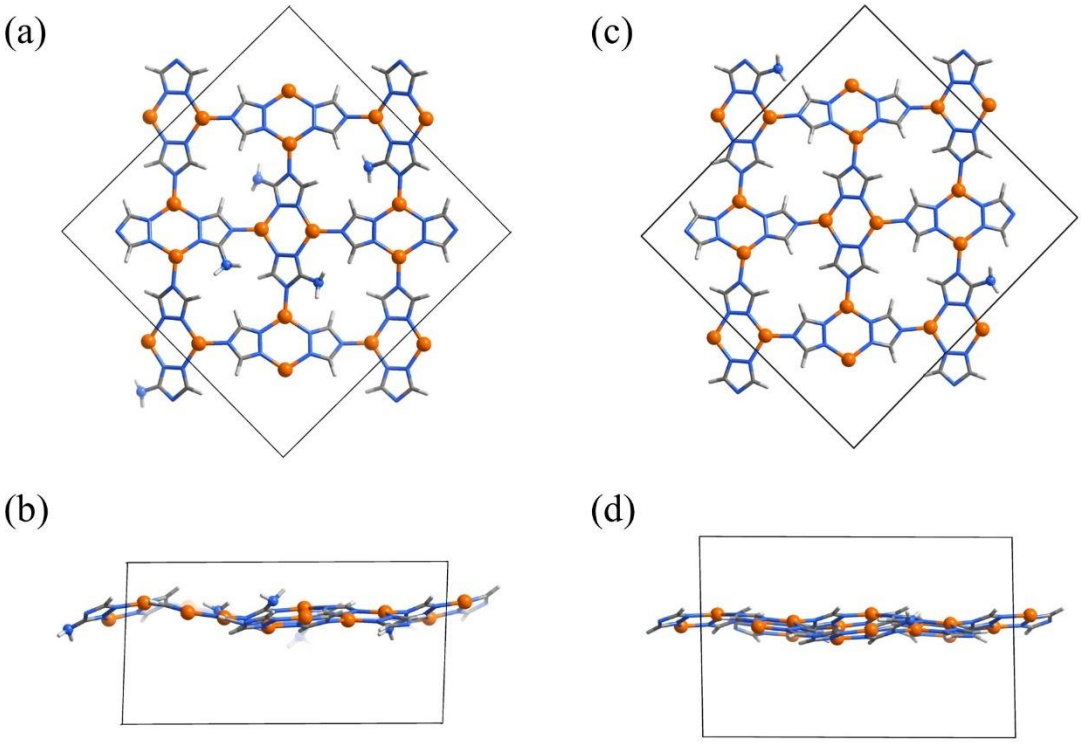

Fig. S30 The model structures of (a,b) ***p*-$A_{31.2}H_{68.8}$**, and (c,d) ***w*-$A_{12.5}H_{87.5}$** for computational calculations at the perspective view perpendicular (a,c) and along (b,d) to the layers.

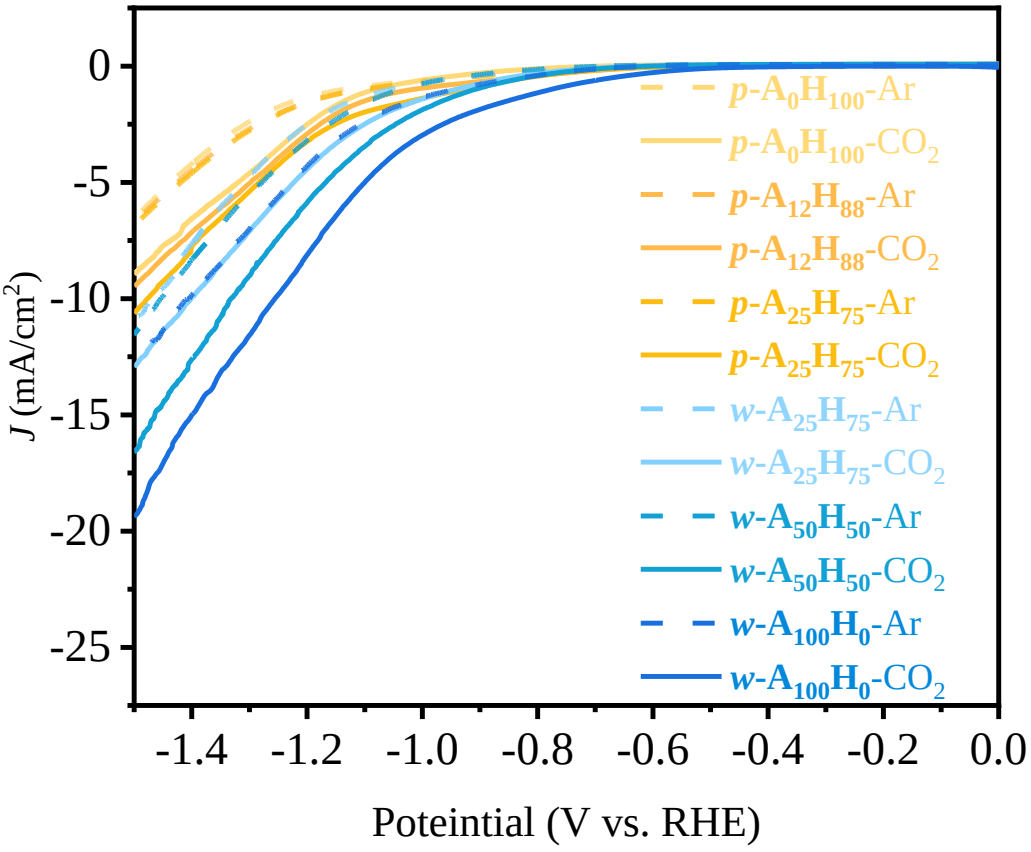

Fig. S31 LSV curves of ***p*-A$_x$H$_{100-x}$** and ***w*-A$_x$H$_{100-x}$**.

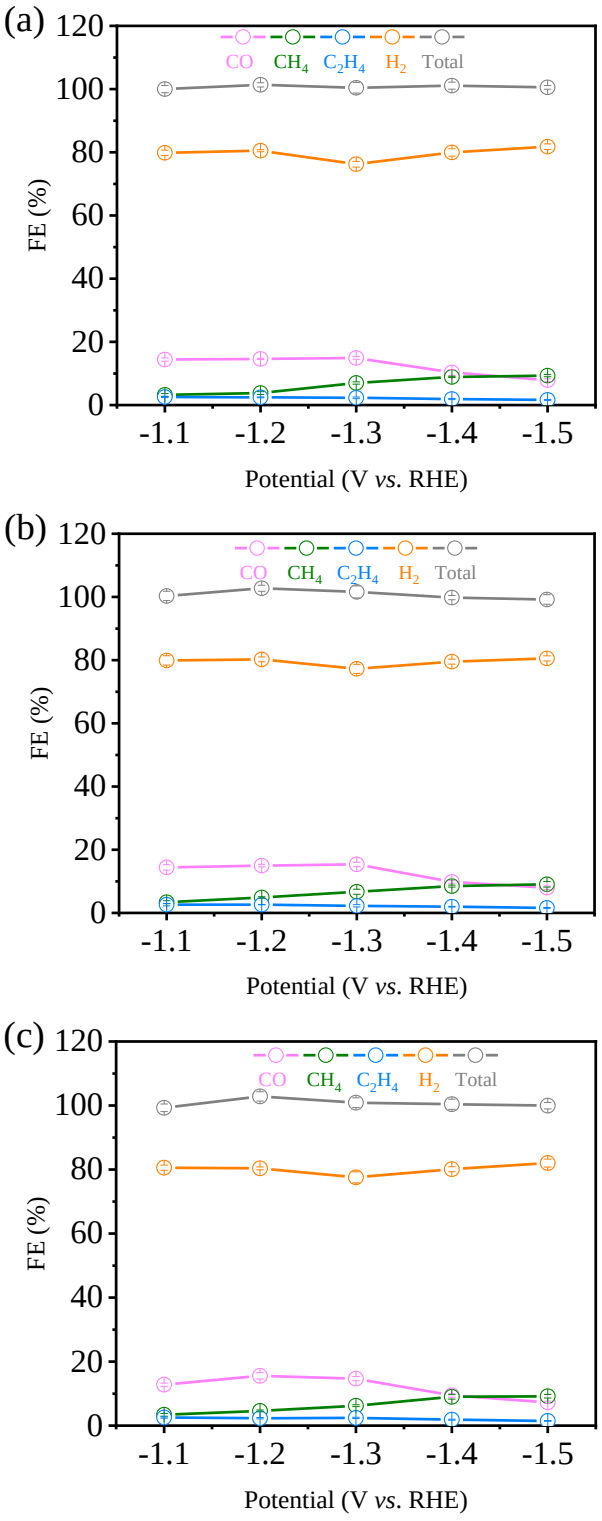

Fig. S32 Potential dependent FE of gas products for the ***p*-A$_{12}$H$_{88}$** samples synthesized in three batches. (a) First, (b) Second, (c) Third batch.

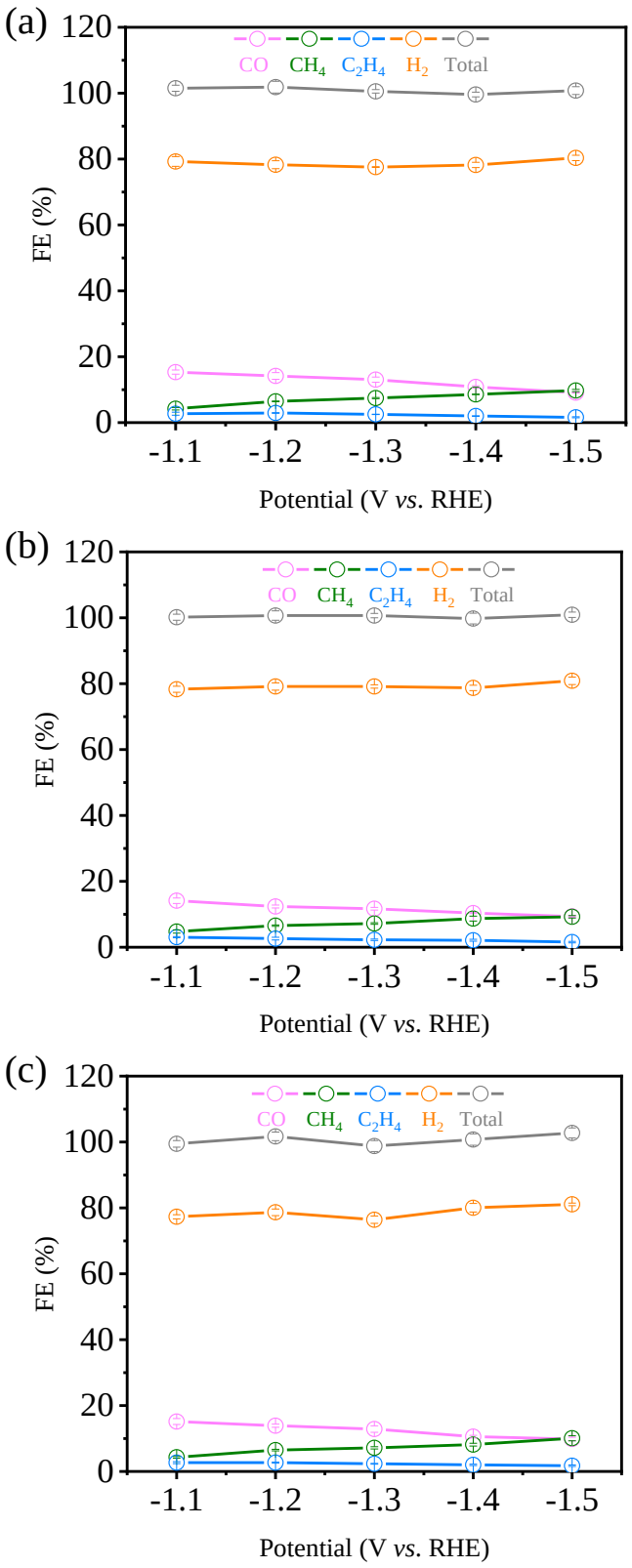

Fig. S33 Potential dependent FE of gas products for the ***p*-A$_{25}$H$_{75}$** samples synthesized in three batches. (a) First, (b) Second, (c) Third batch.

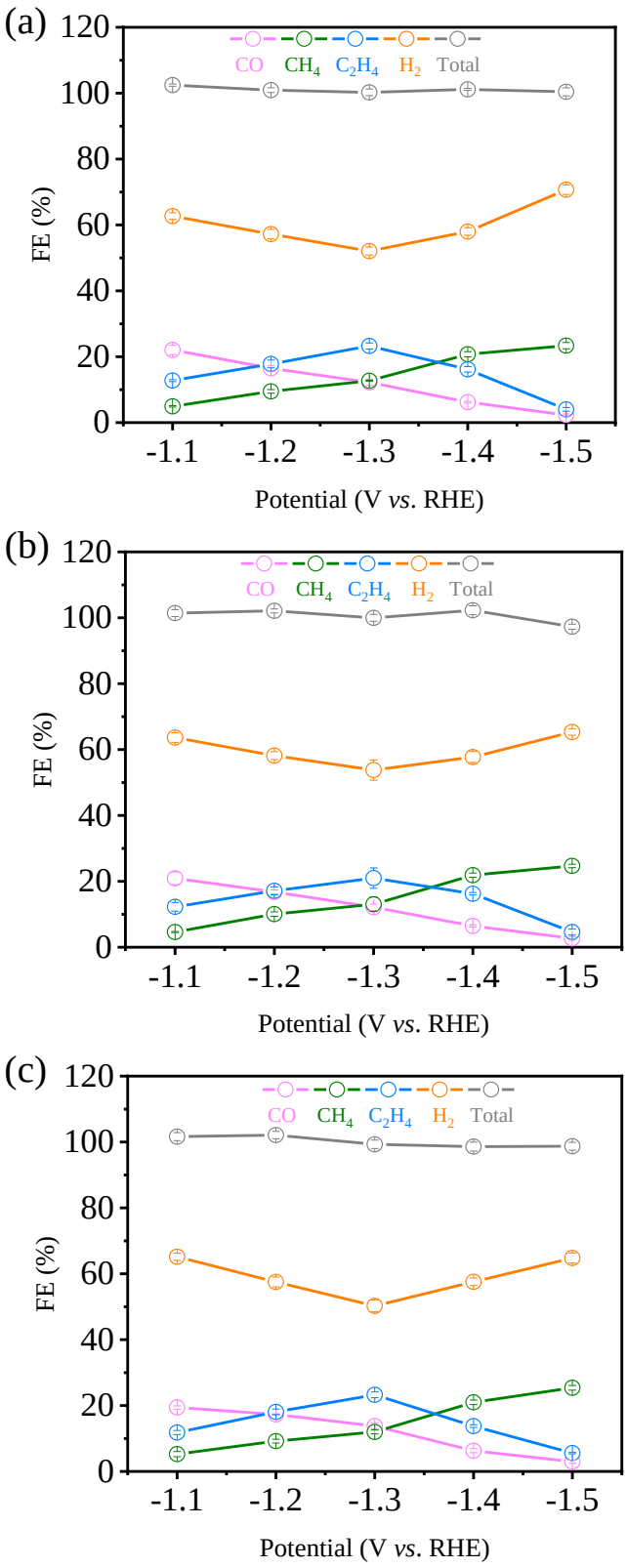

Fig. S34 Potential dependent FE of gas products for the ***w*-A$_{25}$H$_{75}$** samples synthesized in three batches. (a) First, (b) Second, (c) Third batch.

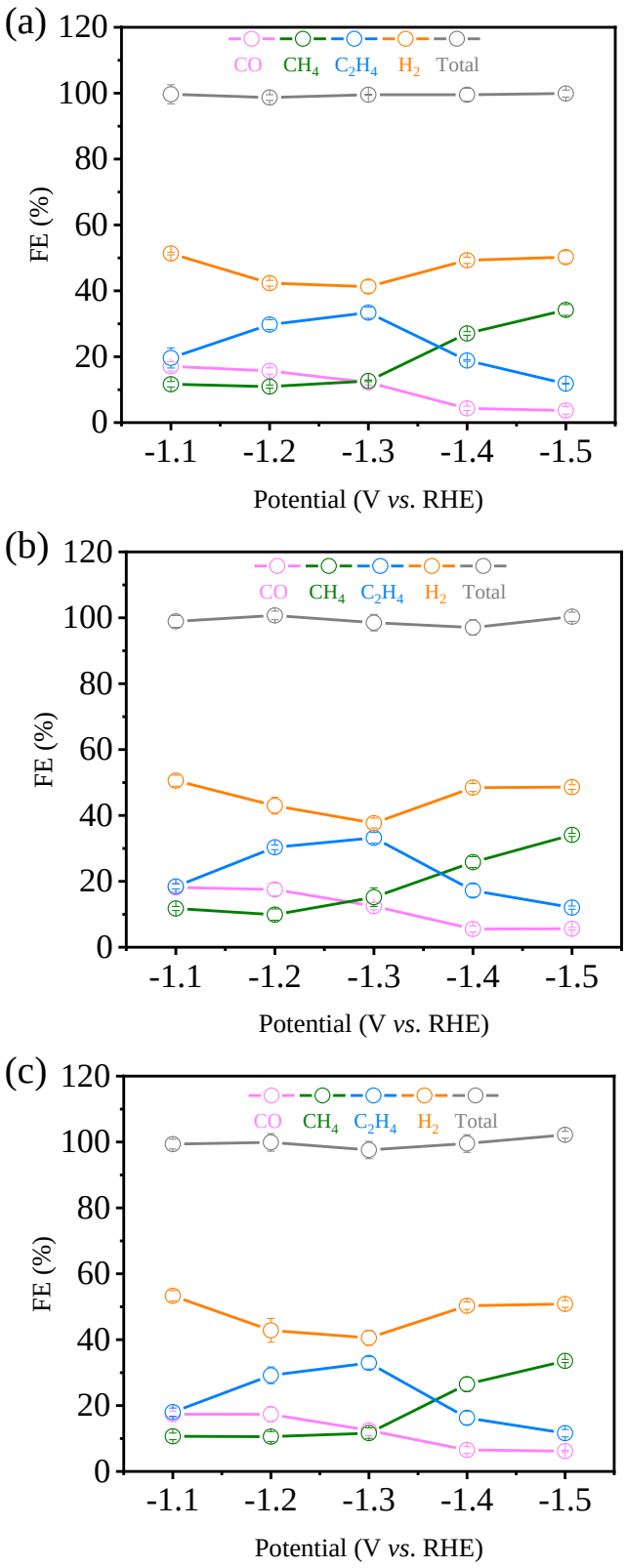

Fig. S35 Potential dependent FE of gas products for the ***w*-A$_{50}$H$_{50}$** samples synthesized in three batches. (a) First, (b) Second, (c) Third batch.

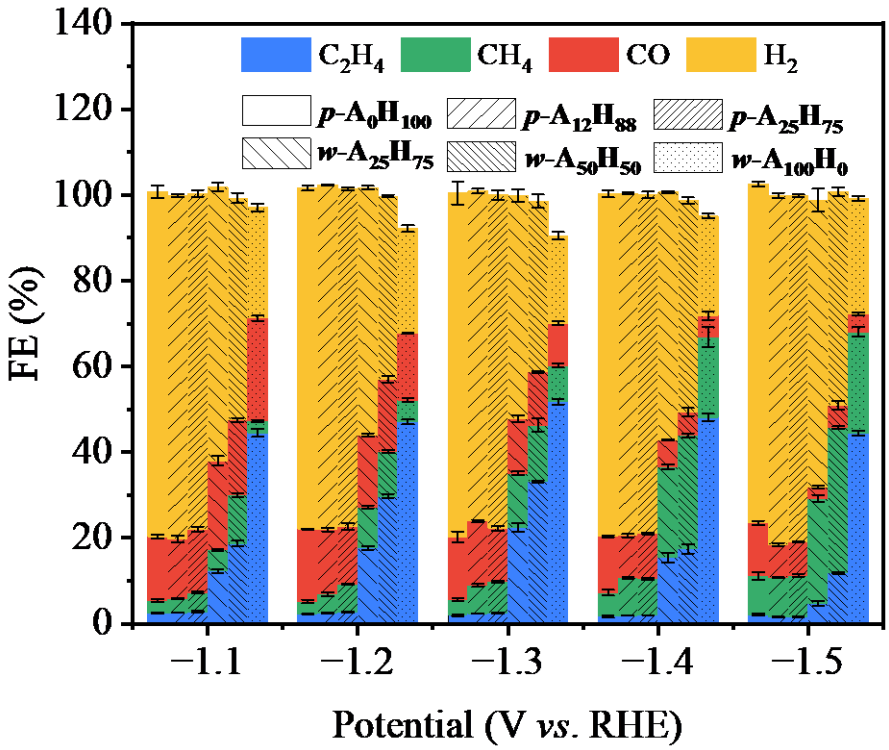

Fig. S36 Potential-dependent FE of gas products for ***p*-A$_x$H$_{100-x}$** and ***w*-A$_x$H$_{100-x}$**.

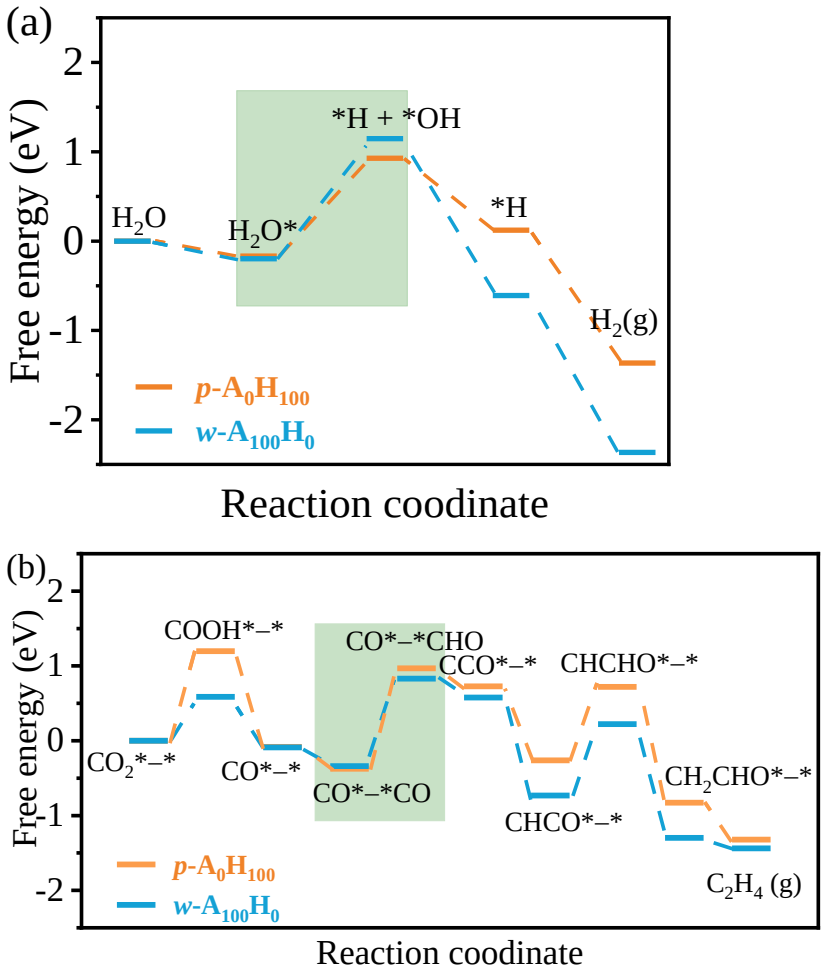

Fig. S37 PDFT-simulated HER/CO_2RR mechanisms for ***p*-A$_0$H$_{100}$** and ***w*-A$_{100}$H$_0$**. (a) Free energy diagram for HER. (b) Free energy diagram for CO_2RR.

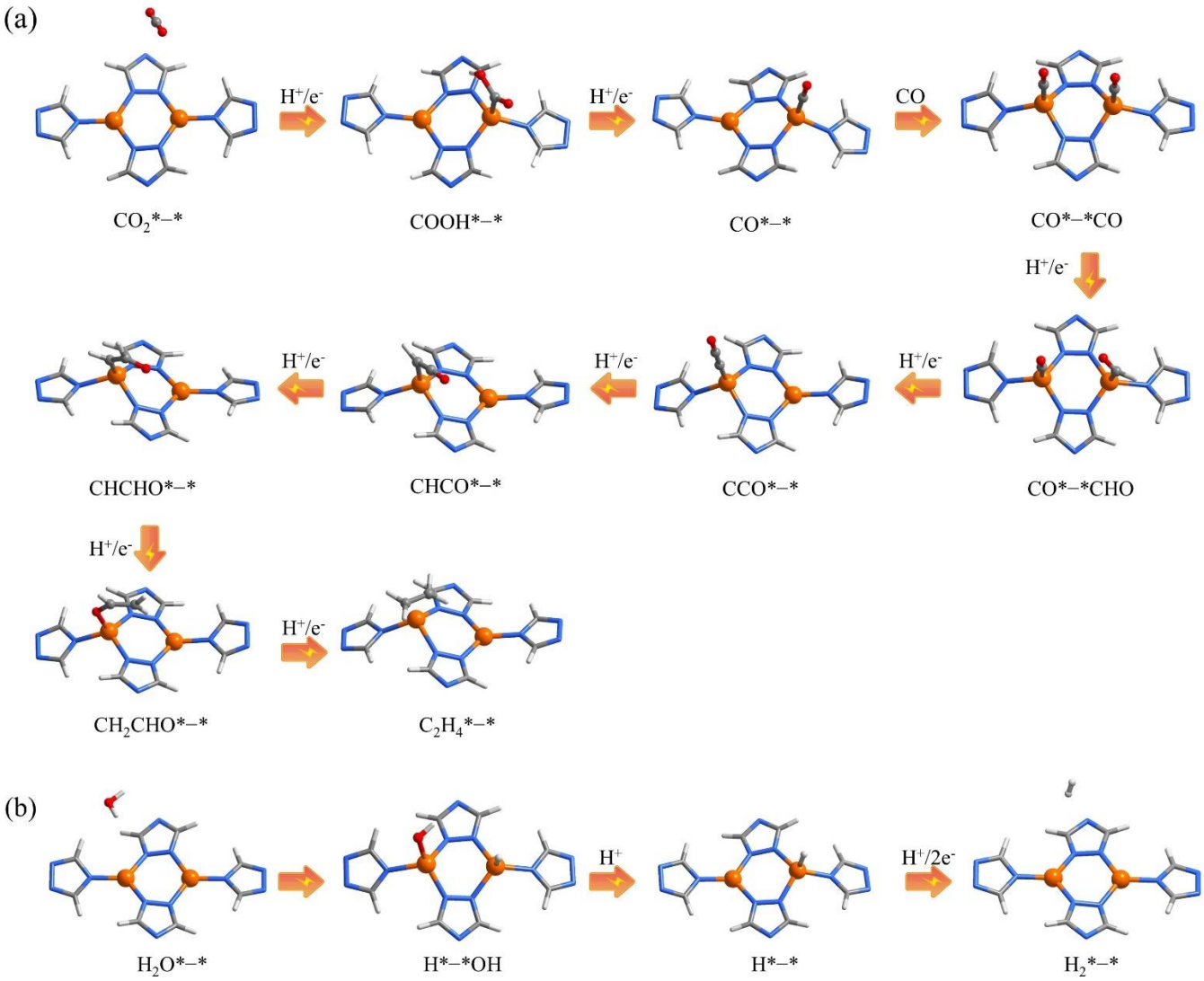

Fig. S38 (a) The C_2H_4 pathway for ***p*-A$_0$H$_{100}$**. (b) The H_2 pathway for ***p*-A$_0$H$_{100}$**.

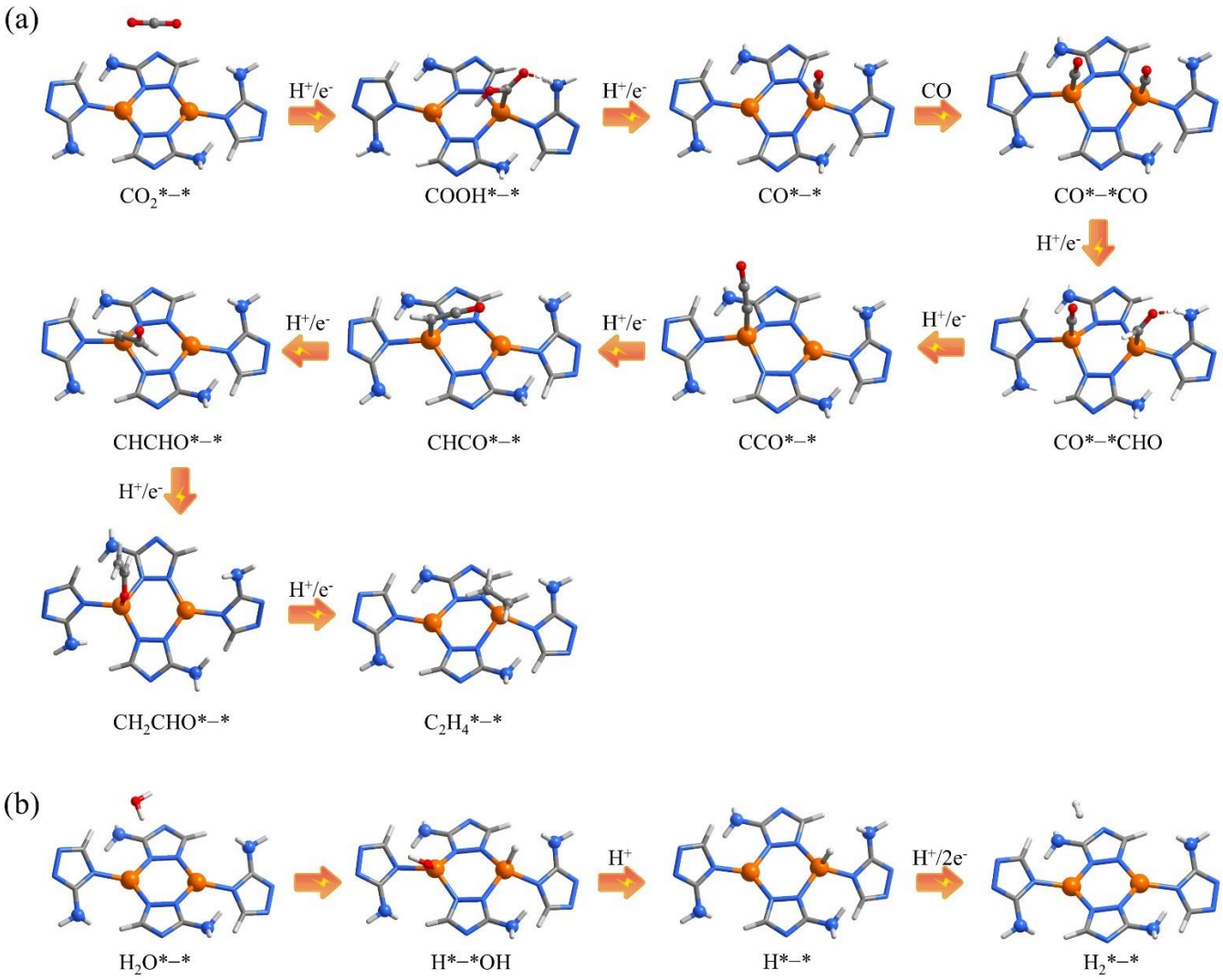

Fig. S39 (a) The C_2H_4 pathway for ***w*-A$_{100}$H$_0$**. (b) The H_2 pathway for ***w*-A$_{100}$H$_0$**.

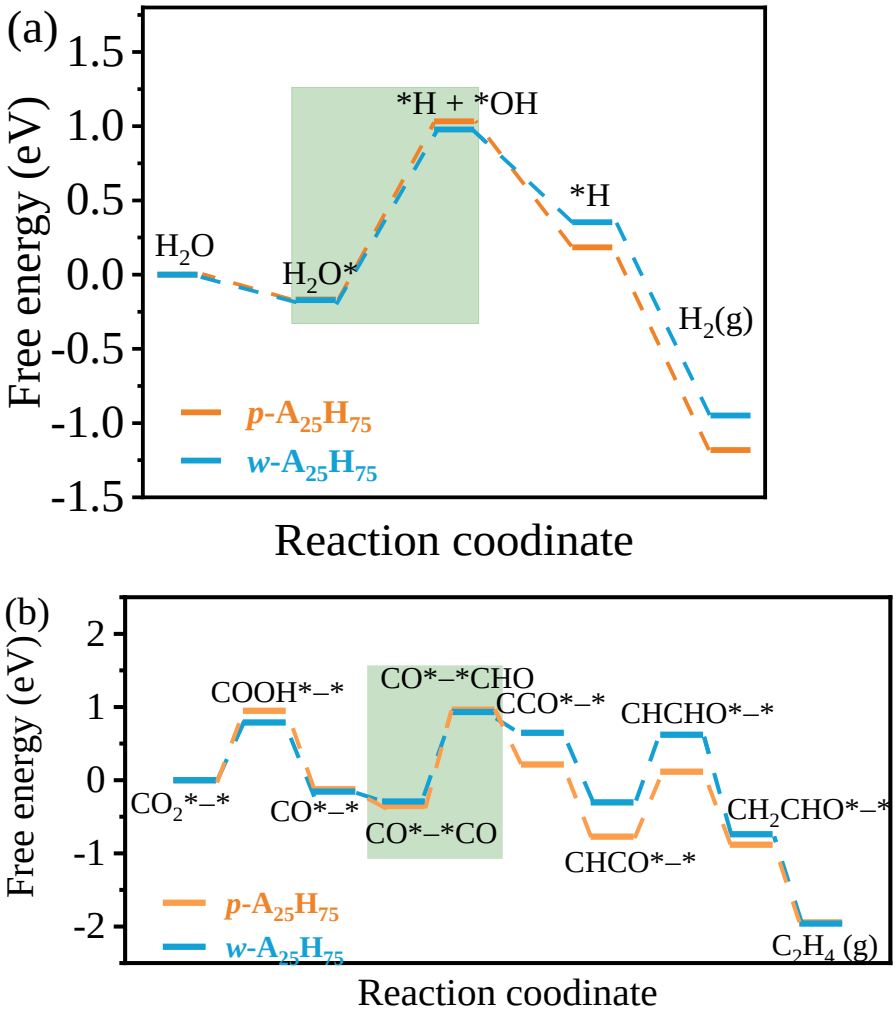

Fig. S40 PDFT-simulated HER/CO_2RR mechanisms for ***p*-A$_{25}$H$_{75}$** and ***w*-A$_{25}$H$_{75}$**. (a) Free energy diagram for HER. (b) Free energy diagram for CO_2RR.

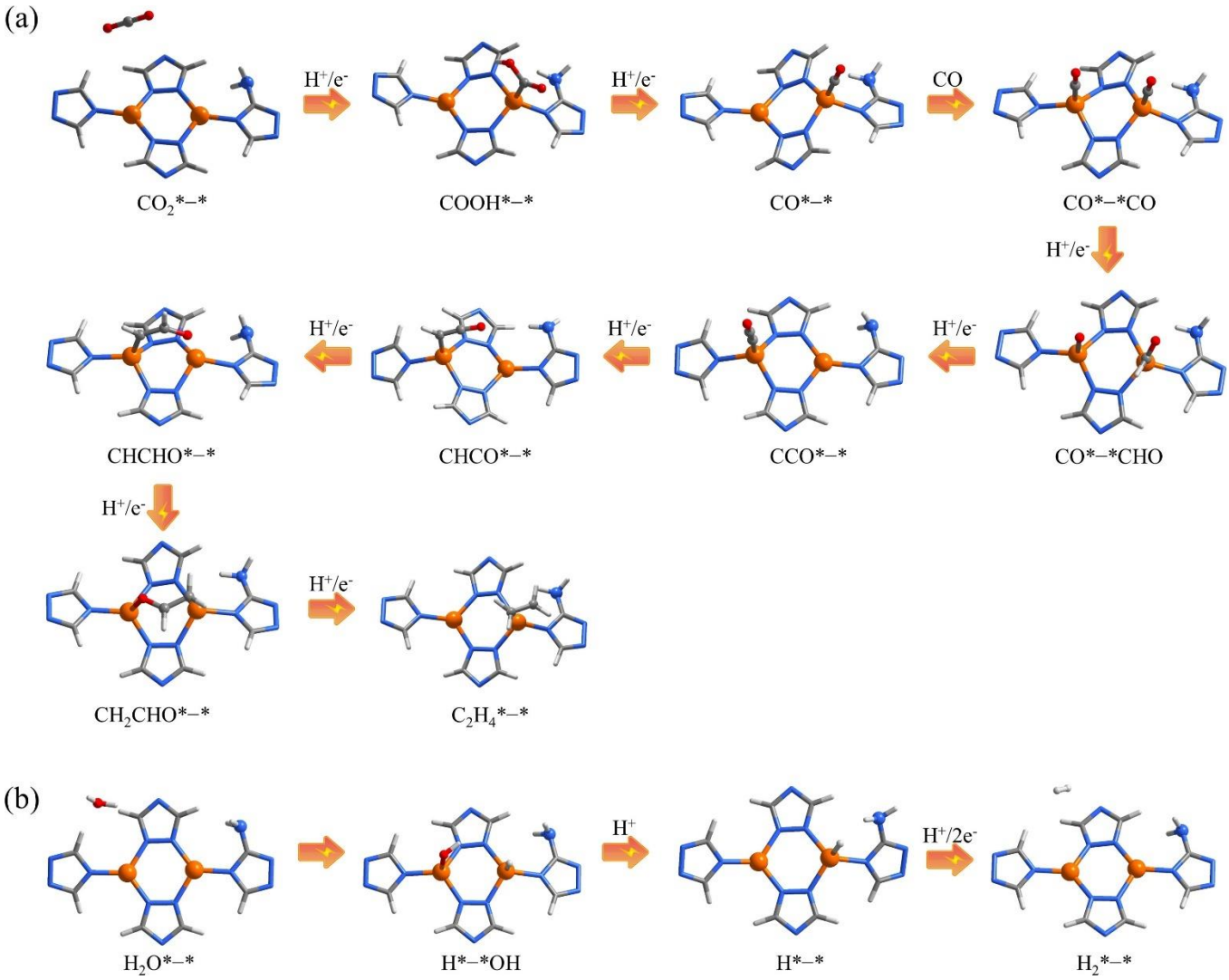

Fig. S41 (a) The C_2H_4 pathway for ***p*-A$_{25}$H$_{75}$**. (b) The H_2 pathway for ***p*-A$_{25}$H$_{75}$**.

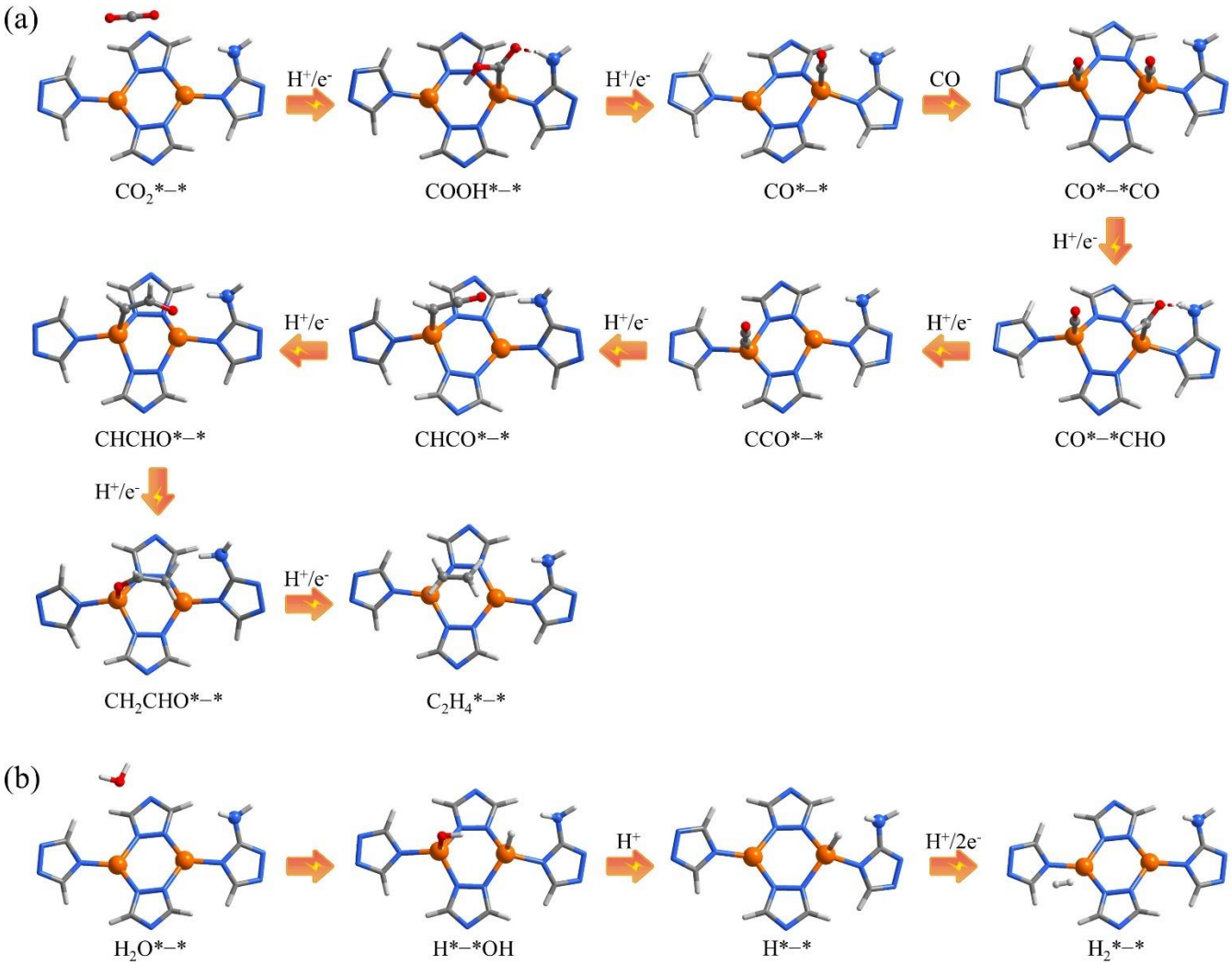

Fig. S42 (a) The C_2H_4 pathway for ***w*-A$_{25}$H$_{75}$**. (b) The H_2 pathway for ***w*-A$_{25}$H$_{75}$**.

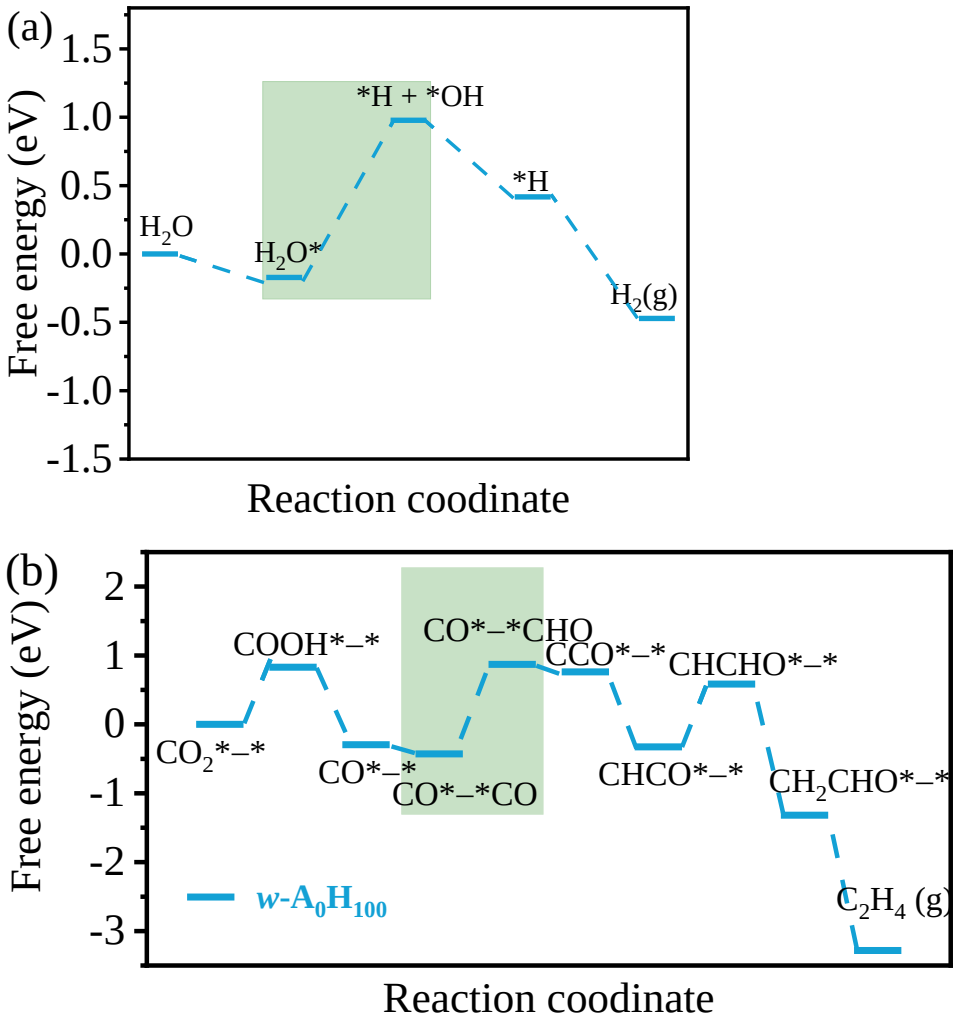

Fig. S43 PDFT-simulated HER/CO_2RR mechanisms for ***w*-A_0H_{100}.** (a) Free energy diagram for HER. (b) Free energy diagram for CO_2RR.

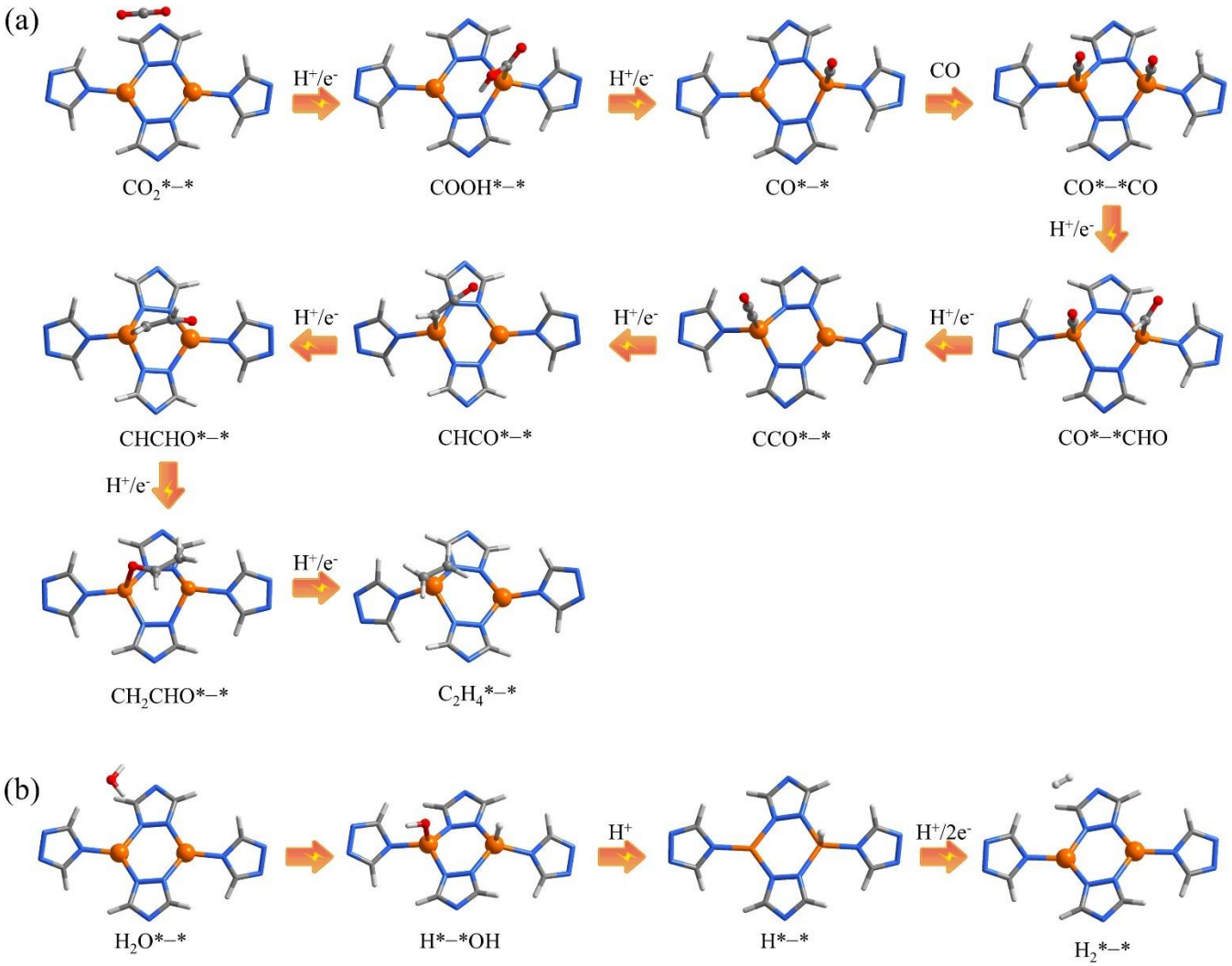

Fig. S44 (a) The C_2H_4 pathway for ***w*-A$_0$H$_{100}$**. (b) The H_2 pathway for ***w*-A$_0$H$_{100}$**.

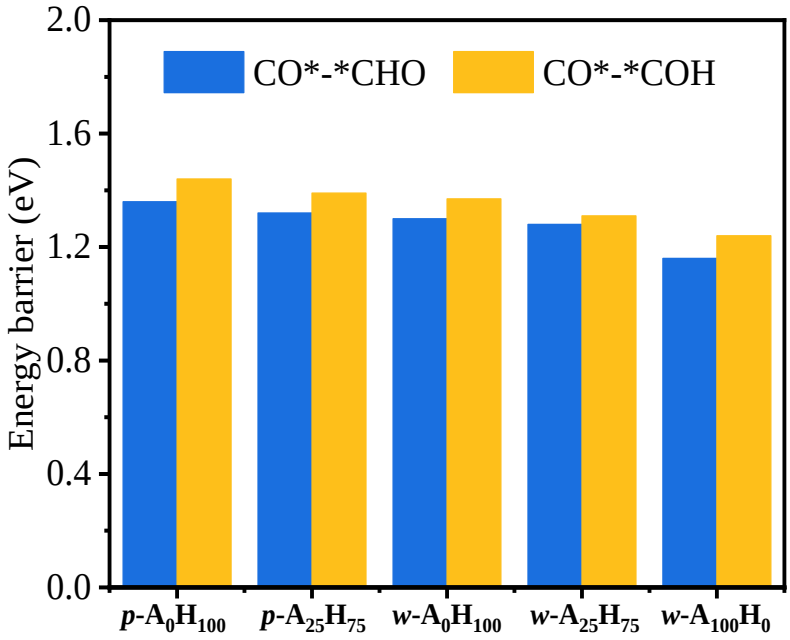

Fig. S45 Comparison of Δ*G* for CO*–*CHO and CO*–*COH. The results show that the energy barriers for CO*–*CO → CO*–*COH (1.44/1.39/1.37/1.31/1.24 eV for ***p*-A$_0$H$_{100}$/*p*-A$_{25}$H$_{75}$/*w*-A$_0$H$_{100}$/*w*-A$_{25}$H$_{75}$/*w*-A$_{100}$H$_0$**, respectively) are higher than those for CO*–*CO → CO*–*CHO (1.36/1.32/1.30/1.28/1.16 eV for ***p*-A$_0$H$_{100}$/*p*-A$_{25}$H$_{75}$/*w*-A$_0$H$_{100}$/*w*-A$_{25}$H$_{75}$/*w*-A$_{100}$H$_0$**, respectively), indicating that the pathway of CO*–*CO → CO*–*CHO is more favorable than that of CO*–*CO → CO*–*COH.

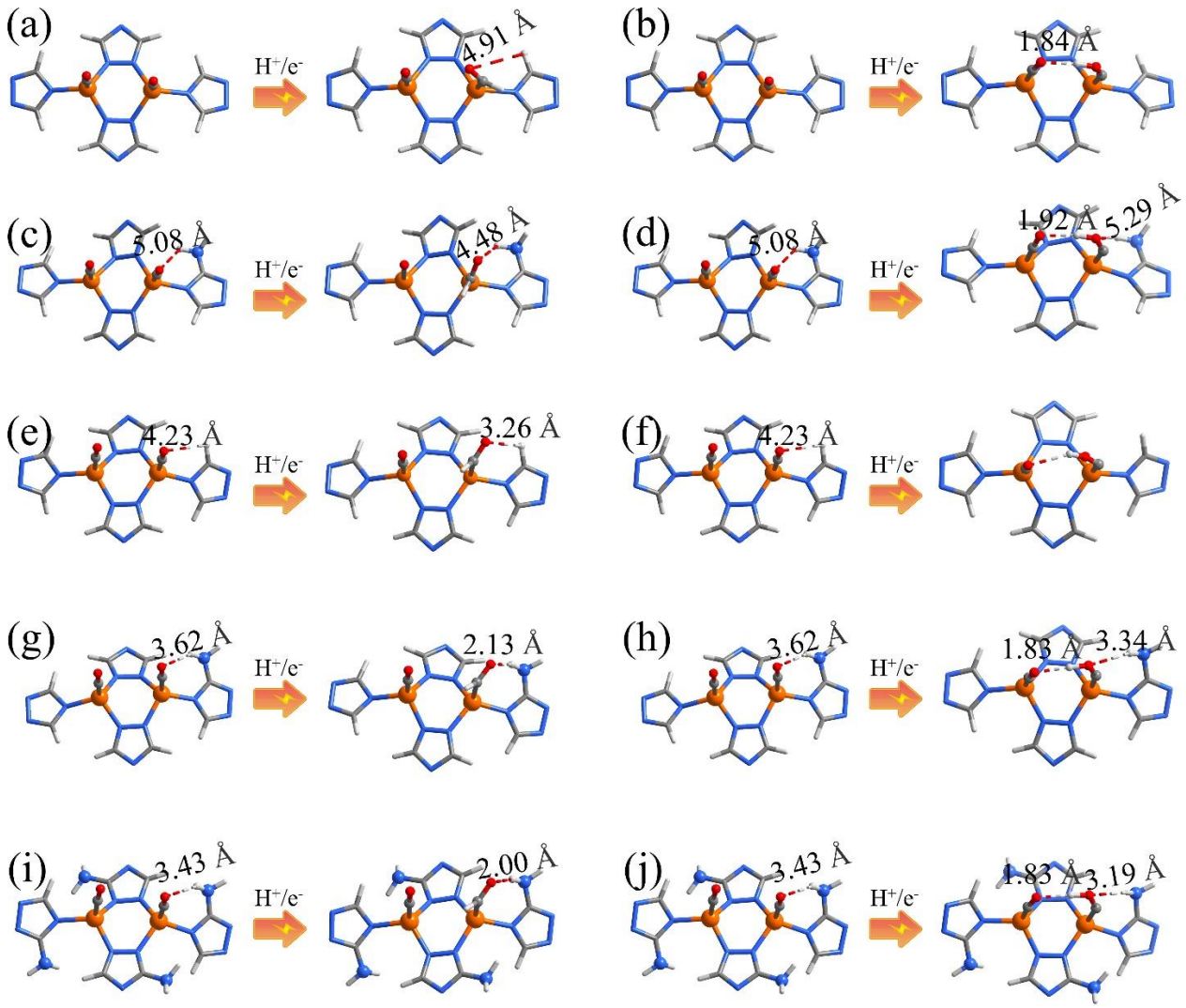

Fig. S46 The structures of the CO*–*CHO/CO*–*COH intermediates for (a,b) ***p*-A$_0$H$_{100}$**, (c,d) ***p*-A$_{25}$H$_{75}$**, (e,f) ***w*-A$_0$H$_{100}$**, (g,h) ***w*-A$_{25}$H$_{75}$** and (i,j) ***w*-A$_{100}$H$_0$**. Notably, the distances between the amino group and *COH are longer than those with *CHO.

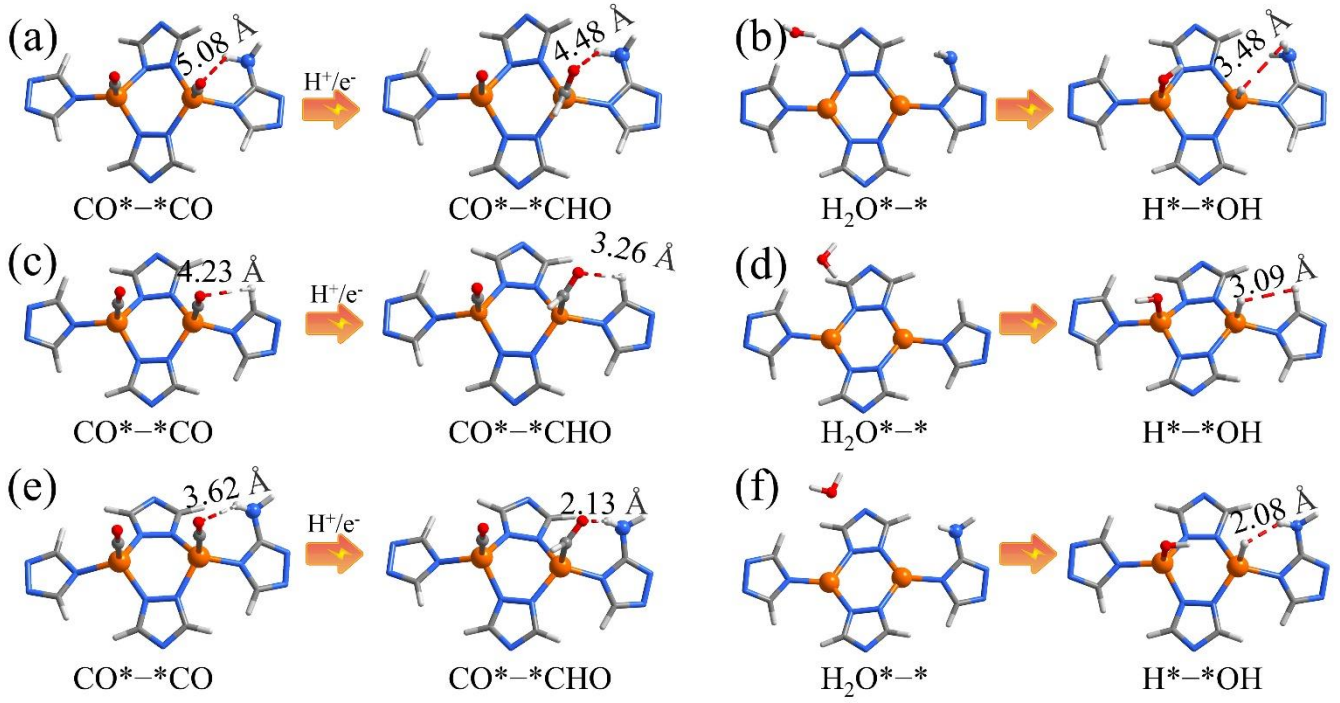

Fig. S47 The structures of the key CO_2RR/HER intermediates for (a,b) ***p*-A$_{25}$H$_{75}$**, (c,d) ***w*-A$_0$H$_{100}$** and (e,f) ***w*-A$_{25}$H$_{75}$**.

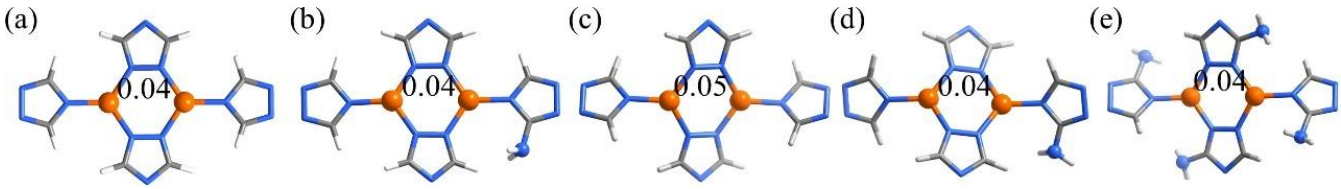

Fig. S48 The Mulliken population analysis of (a) ***p*-A$_0$H$_{100}$**, (b) ***p*-A$_{25}$H$_{75}$**, (c) ***w*-A$_0$H$_{100}$**, (d) ***w*-A$_{25}$H$_{75}$** and (e) ***w*-A$_{100}$H$_0$** from computational calculations.

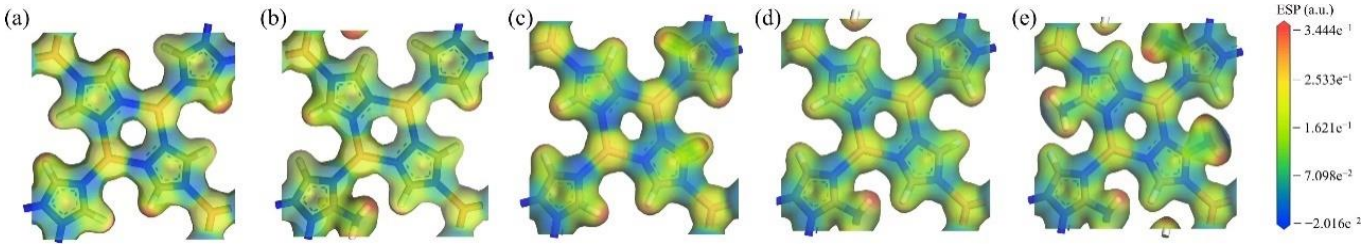

Fig. S49 The electrostatic potential of (a) ***p*-A$_0$H$_{100}$**, (b) ***p*-A$_{25}$H$_{75}$**, (c) ***w*-A$_0$H$_{100}$**, (d) ***w*-A$_{25}$H$_{75}$** and (e) ***w*-A$_{100}$H$_0$** from computational calculations.

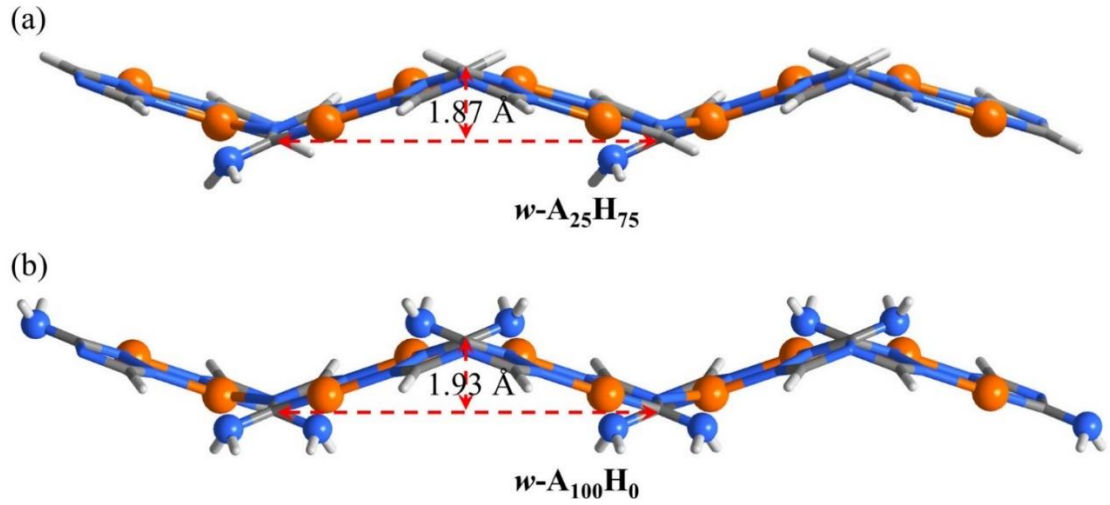

Fig. S50 The PDFT-calculated single-layer structure of (a) ***w*-A$_{25}$H$_{75}$** and (b) ***w*-A$_{100}$H$_0$**

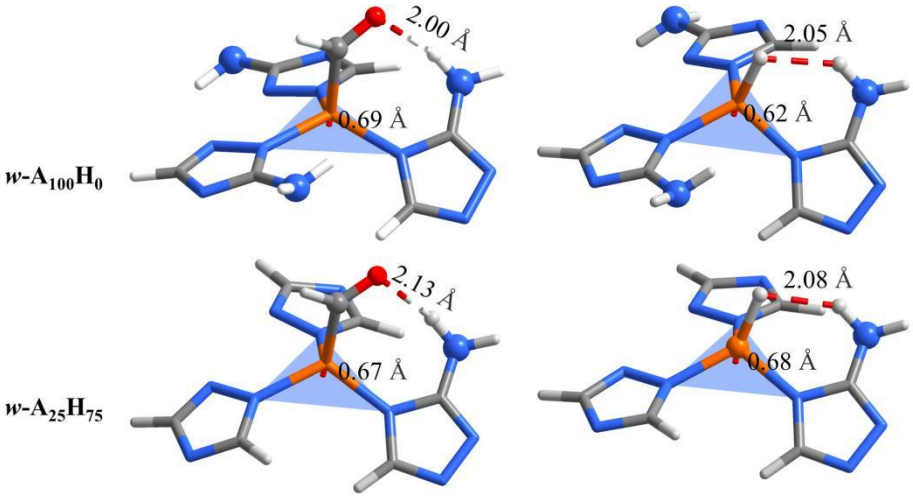

Fig. S51 The coordination unit of *CHO or *H on ***w*-A$_{100}$H$_0$**.and ***w*-A$_{25}$H$_{75}$**.

Table S1. The detail values of faradic efficiency catalyzed by [Cu(tz)].

First batch (V *vs.* RHE)		CO (%)	CH_4 (%)	C_2H_4 (%)	H_2 (%)	Total (%)
–1.1	Electrode 1	5.6	3.0	2.2	92.4	103.1
–1.2	Electrode 1	5.6	1.6	1.7	91.6	100.5
–1.3	Electrode 1	4.0	1.9	2.1	91.0	99.1
–1.4	Electrode 1	3.9	5.0	2.4	90.1	101.4
–1.5	Electrode 1	2.2	4.2	2.0	92.9	101.3
Second batch (V *vs.* RHE)		CO (%)	CH_4 (%)	C_2H_4 (%)	H_2 (%)	Total (%)
–1.1	Electrode 2	6.3	2.7	3.1	89.9	101.9
–1.2	Electrode 2	5.1	2.0	2.4	92.7	102.1
–1.3	Electrode 2	4.8	2.1	1.5	93.1	101.5
–1.4	Electrode 2	4.3	4.5	1.7	91.1	101.6
–1.5	Electrode 2	2.5	3.4	1.2	93.6	100.6
Third batch (V *vs.* RHE)		CO (%)	CH_4 (%)	C_2H_4 (%)	H_2 (%)	Total (%)
–1.1	Electrode 3	6.3	2.0	1.5	90.6	100.4
–1.2	Electrode 3	5.3	1.9	2.0	92.4	101.6
–1.3	Electrode 3	4.5	2.8	1.7	92.5	101.5
–1.4	Electrode 3	4.4	3.2	1.4	90.8	99.8
–1.5	Electrode 3	1.8	3.1	1.4	94.1	100.5
Three batch (V *vs.* RHE)		CO (%)	CH_4 (%)	C_2H_4 (%)	H_2 (%)	Total (%)
Average value	–1.1	6.0±0.3	2.6±0.4	2.3±0.7	90.9±1.0	101.8±1.1
	–1.2	5.3±0.2	1.8±0.1	2.0±0.3	92.3±0.5	101.4±0.7
	–1.3	4.4±0.3	2.3±0.4	1.8±0.3	92.2±0.9	100.7±1.1
	–1.4	4.2±0.2	4.3±0.8	1.8±0.4	90.7±0.4	101.0±0.8
	–1.5	2.2±0.2	3.6±0.5	1.5±0.3	93.5±0.5	100.8±0.4

Table S2. The detail values of faradic efficiency catalyzed by [Cu(atz)].

First batch (V *vs.* RHE)		CO (%)	CH_4 (%)	C_2H_4 (%)	H_2 (%)	Total (%)
–1.1	Electrode 1	10.9	5.7	29.9	54.8	101.2
–1.2	Electrode 1	7.1	7.8	32.8	54.5	102.3
–1.3	Electrode 1	5.7	9.8	35.7	50.9	102.0
–1.4	Electrode 1	4.5	12.1	24.8	61.8	103.2
–1.5	Electrode 1	3.6	13.2	17.6	70.0	104.3
Second batch (V *vs.* RHE)		CO (%)	CH_4 (%)	C_2H_4 (%)	H_2 (%)	Total (%)
–1.1	Electrode 2	10.4	6.5	29.1	54.4	100.5
–1.2	Electrode 2	8.3	7.3	31.2	54.9	101.8
–1.3	Electrode 2	6.1	8.0	32.0	51.5	97.6
–1.4	Electrode 2	4.9	13.1	24.2	58.0	100.1
–1.5	Electrode 2	3.9	12.3	18.1	67.7	102.7
Third batch (V *vs.* RHE)		CO (%)	CH_4 (%)	C_2H_4 (%)	H_2 (%)	Total (%)
–1.1	Electrode 3	12.4	6.2	30.2	52.1	100.9
–1.2	Electrode 3	6.9	6.4	32.1	55.4	100.8
–1.3	Electrode 3	5.9	7.1	32.4	51.7	97.1
–1.4	Electrode 3	5.0	13.0	23.8	61.0	102.7
–1.5	Electrode 3	4.0	13.8	17.8	65.5	101.1
Three batch (V *vs.* RHE)		CO (%)	CH_4 (%)	C_2H_4 (%)	H_2 (%)	Total (%)
Average value	–1.1	11.2±0.9	6.1±0.4	29.7±0.5	53.8±1.2	100.9±0.3
	–1.2	7.4±0.6	7.2±0.6	32.0±0.7	55.0±0.4	101.6±0.6
	–1.3	5.9±0.2	8.3±1.1	33.3±1.7	51.4±0.4	98.9±2.2
	–1.4	4.8±0.2	12.7±0.5	24.3±0.4	60.3±1.6	102.0±1.4
	–1.5	3.8±0.2	13.1±0.6	17.8±0.2	67.7±1.8	102.5±1.4

Table S3. The detail values of faradic efficiency catalyzed by ***p*-A_0H_{100}**.

First batch (V *vs*. RHE)		CO (%)	CH_4 (%)	C_2H_4 (%)	H_2 (%)	Total (%)
–1.1	Electrode 1	14.7	3.4	2.8	80.8	101.7
	Electrode 2	15.8	3.8	2.2	78.1	99.9
	Electrode 3	14.5	3.5	2.3	79.3	99.6
	Average value	15.0±0.6	3.6±0.2	2.4±0.3	79.4±1.10	100.4±1.0
–1.2	Electrode 1	15.6	3.2	2.3	80.6	101.6
	Electrode 2	19.3	3.6	2.2	79.9	105.0
	Electrode 3	15.7	3.4	2.1	80.5	101.6
	Average value	16.9±1.7	3.4±0.2	2.2±0.1	80.3±0.3	102.8±1.6
–1.3	Electrode 1	15.5	2.7	1.7	75.4	95.4
	Electrode 2	15.7	3.2	1.2	76.5	96.7
	Electrode 3	16.6	3.8	2.2	78.4	100.9
	Average value	15.9±0.5	3.2±0.4	1.7±0.34	76.8±1.2	97.6±2.4
–1.4	Electrode 1	11.4	6.3	1.4	79.8	99.0
	Electrode 2	14.2	5.1	1.3	78.5	99.1
	Electrode 3	13.8	4.1	1.1	79.4	98.3
	Average value	13.1±1.2	5.2±0.9	1.3±0.1	79.2±0.6	98.8±0.3
–1.5	Electrode 1	11.9	7.5	1.6	79.6	100.5
	Electrode 2	12.3	7.7	1.2	79.2	100.3
	Electrode 3	11.5	8.9	1.2	80.7	102.3
	Average value	11.9±0.3	8.0±0.6	1.3±0.2	79.8±0.6	101.0±0.9
Second batch (V *vs*. RHE)		CO (%)	CH_4 (%)	C_2H_4 (%)	H_2 (%)	Total (%)
–1.1	Electrode 1	13.8	2.9	2.6	80.5	99.7
	Electrode 2	16.4	2.5	2.4	77.6	98.9
	Electrode 3	16.3	2.6	2.0	80.3	101.3
	Average value	15.5±1.3	2.7±0.2	2.3±0.2	79.5±1.4	100.0±1.3
–1.2	Electrode 1	17.4	2.2	2.1	77.6	99.2
	Electrode 2	17.9	2.7	2.2	79.8	102.6
	Electrode 3	16.0	2.5	2.3	79.0	99.8
	Average value	17.1±0.8	2.5±0.2	2.2±0.2	78.8±1.0	100.5±1.5
–1.3	Electrode 1	13.2	4.2	3.3	78.4	99.2
	Electrode 2	13.1	3.5	1.5	82.2	100.4
	Electrode 3	12.5	4.0	1.7	81.6	99.8
	Average value	12.9±0.4	3.9±0.4	2.2±0.8	80.8±1.8	99.8±0.7
–1.4	Electrode 1	12.6	4.9	2.2	79.0	98.6
	Electrode 2	13.3	5.1	1.5	79.4	99.3
	Electrode 3	12.9	5.0	2.2	79.6	99.6
	Average value	12.9±0.6	5.0±0.2	1.9±0.4	79.3±0.2	99.2±0.7
–1.5	Electrode 1	12.6	9.1	2.2	79.0	102.9
	Electrode 2	11.6	9.1	0.8	80.9	102.4
	Electrode 3	12.6	8.2	2.3	76.6	99.8
	Average value	12.3±1.1	8.8±0.4	1.8±0.7	78.8±1.8	101.7±1.5
Third batch (V *vs*. RHE)		CO (%)	CH_4 (%)	C_2H_4 (%)	H_2 (%)	Total (%)
–1.1	Electrode 1	14.9	2.8	2.6	81.8	102.0
	Electrode 2	14.2	2.7	2.7	83.3	102.8
	Electrode 3	13.9	2.5	2.3	82.2	100.9
	Average value	14.3±0.5	2.6±0.2	2.5±0.2	82.4±0.7	101.9±1.0
–1.2	Electrode 1	16.6	3.7	2.5	80.7	103.5
	Electrode 2	17.3	2.5	2.0	78.7	100.5
	Electrode 3	16.5	2.7	2.6	79.1	100.8
	Average value	16.8±0.4	2.9±0.6	2.4±0.3	79.5±0.9	101.6±1.4
–1.3	Electrode 1	15.2	4.3	2.7	80.4	102.4
	Electrode 2	14.4	3.5	1.8	84.4	104.2
	Electrode 3	15.6	3.6	1.6	84.7	105.4
	Average value	15.1±0.5	3.8±0.3	2.0±0.5	83.2±2.2	104.0±1.6
–1.4	Electrode 1	13.2	8.2	2.3	80.2	103.9
	Electrode 2	13.4	7.0	1.9	80.1	102.4
	Electrode 3	13.8	4.3	1.5	82.8	102.4
	Average value	13.5±0.3	6.5±1.7	1.9±0.3	81.0±1.3	102.9±1.1
–1.5	Electrode 1	13.6	9.7	2.1	78.9	104.2
	Electrode 2	12.7	9.2	2.0	78.8	102.7
	Electrode 3	12.8	11.7	1.4	78.1	104.0
	Average value	13.0±0.4	10.2±1.2	1.8±0.3	78.6±0.5	103.6±0.8
Three batch (V *vs*. RHE)		CO (%)	CH_4 (%)	C_2H_4 (%)	H_2 (%)	Total (%)
Average value	–1.1	14.9±0.5	3.0±0.4	2.4±0.1	80.4±1.4	100.7±0.8
	–1.2	16.9±0.1	2.9±0.4	2.3±0.1	79.5±0.6	101.6±0.9
	–1.3	14.6±1.3	3.7±0.3	2.0±0.2	80.2±2.6	100.5±2.7
	–1.4	13.2±0.2	5.6±0.7	1.7±0.3	79.9±0.8	100.3±1.8
	–1.5	12.4±0.5	9.0±0.9	2.1±0.2	79.1±0.5	102.1±1.1

Table S4. The detailed values of faradic efficiency catalyzed by ***w*-A$_{100}$H$_0$**.

First batch (V *vs*. RHE)		CO (%)	CH_4 (%)	C_2H_4 (%)	H_2 (%)	Total (%)
–1.1	Electrode 1	23.6	2.7	42.2	25.7	94.2
	Electrode 2	21.5	3.8	48.9	22.9	97.1
	Electrode 3	24.3	2.6	45.5	25.3	97.7
	Average value	23.1±1.2	3.04±0.6	45.5±2.7	24.6±1.23	96.4±1.5
–1.2	Electrode 1	17.2	4.0	43.5	24.8	89.4
	Electrode 2	14.5	6.2	50.4	20.8	91.8
	Electrode 3	14.6	7.3	48.7	24.6	95.2
	Average value	15.4±1.3	5.8±1.4	47.5±2.9	23.4±1.8	92.1±2.4
–1.3	Electrode 1	8.6	8.7	48.7	22.5	96.5
	Electrode 2	10.9	8.7	54.1	16.6	88.7
	Electrode 3	11.8	9.5	51.5	18.9	91.7
	Average value	10.4±1.3	9.0±0.4	51.4±2.2	19.3±2.5	92.3±3.2
–1.4	Electrode 1	4.9	19.8	44.3	27.5	96.5
	Electrode 2	3.0	16.4	50.2	19.1	88.7
	Electrode 3	3.3	19.6	47.4	21.4	91.7
	Average value	3.7±0.9	18.6±1.6	47.3±2.4	22.7±3.5	92.3±3.2
–1.5	Electrode 1	4.6	21.8	42.0	28.2	98.9
	Electrode 2	3.0	17.7	47.0	26.9	97.1
	Electrode 3	3.9	28.1	43.9	27.9	99.1
	Average value	3.8±0.7	22.5±5.2	44.3±2.1	27.7±0.6	98.3±0.9
Second batch (V *vs*. RHE)		CO (%)	CH_4 (%)	C_2H_4 (%)	H_2 (%)	Total (%)
–1.1	Electrode 1	25.3	2.3	43.2	25.5	96.4
	Electrode 2	22.2	2.5	46.5	26.7	97.9
	Electrode 3	25.8	2.5	44.4	26.3	98.9
	Average value	24.4±1.7	2.4±0.1	44.7±1.4	26.2±0.5	94.6±1.4
–1.2	Electrode 1	17.0	3.4	45.3	25.3	90.9
	Electrode 2	13.1	5.0	48.0	25.3	91.5
	Electrode 3	17.3	5.5	45.6	25.4	93.8
	Average value	15.8±1.9	4.7±0.9	46.3±1.2	25.3±0.4	92.0±1.3
–1.3	Electrode 1	8.5	8.6	52.5	19.3	88.9
	Electrode 2	11.7	8.8	50.4	18.9	89.7
	Electrode 3	9.1	8.4	50.8	22.9	91.2
	Average value	9.8±1.4	8.6±0.1	51.2±1.0	20.4±1.8	89.9±1.3
–1.4	Electrode 1	5.2	22.2	49.1	22.5	98.9
	Electrode 2	5.2	22.4	48.3	24.0	99.8
	Electrode 3	4.9	20.4	46.0	25.4	96.7
	Average value	5.1±0.2	21.7±0.9	47.8±1.3	23.9±1.2	98.5±1.5
–1.5	Electrode 1	4.8	24.6	44.4	26.7	100.5
	Electrode 2	4.3	25.9	42.5	25.2	97.9
	Electrode 3	4.6	24.7	44.4	26.6	100.4
	Average value	4.6±0.2	25.1±0.7	43.8±1.1	26.2±0.7	99.6±1.5
Third batch (V *vs*. RHE)		CO (%)	CH_4 (%)	C_2H_4 (%)	H_2 (%)	Total (%)
–1.1	Electrode 1	25.9	2.8	44.8	25.2	98.7
	Electrode 2	23.4	3.7	43.0	27.2	97.3
	Electrode 3	23.6	2.3	42.0	27.5	95.5
	Average value	24.3±1.4	2.9±0.6	43.3±1.2	26.6±1.0	97.1±1.4
–1.2	Electrode 1	17.4	3.5	46.4	23.4	90.6
	Electrode 2	16.4	5.4	19.9	23.4	90.1
	Electrode 3	12.8	5.7	45.7	26.8	91.0
	Average value	15.5±2.0	4.9±1.0	47.3±1.9	24.5±1.6	92.2±2.0
–1.3	Electrode 1	11.4	6.6	51.8	18.8	88.7
	Electrode 2	8.5	6.1	55.4	20.4	90.3
	Electrode 3	8.4	10.7	50.8	25.1	95.0
	Average value	9.4±1.4	7.8±2.1	52.7±2.0	21.4±2.7	91.3±2.8
–1.4	Electrode 1	6.4	22.4	49.3	21.0	92.1
	Electrode 2	5.2	23.9	51.9	20.7	93.9
	Electrode 3	7.1	24.0	46.6	27.5	97.7
	Average value	6.2±0.8	23.4±0.9	49.2±2.2	23.1±3.1	94.6±2.3
–1.5	Electrode 1	4.7	15.6	44.8	26.3	98.2
	Electrode 2	3.1	14.0	45.3	27.7	100.0
	Electrode 3	4.1	19.6	45.2	27.7	100.3
	Average value	4.0±0.7	16.4±2.9	45.1±0.5	27.3±0.7	99.7±1.4
Three batch (V *vs*. RHE)		CO (%)	CH_4 (%)	C_2H_4 (%)	H_2 (%)	Total (%)
Average value	–1.1	24.0±0.6	2.8±0.3	44.5±0.9	25.8±0.9	97.1±0.6
	–1.2	15.6±0.2	5.1±0.5	47.0±0.6	24.4±0.8	92.1±0.1
	–1.3	9.9±0.4	8.5±0.5	51.8±0.6	20.4±0.9	90.5±0.6
	–1.4	5.0±1.0	18.8±2.3	48.1±0.8	23.2±0.5	95.1±2.6
	–1.5	4.1±0.3	23.7±1.1	44.4±0.5	27.0±0.6	99.2±0.6

Table S5. Comparison of the electrocatalytic performances of benchmark catalysts.

Catalyst	E (V *vs.* RHE)	C_2H_4 (%)	Stability / h	After CO_2RR	Electrolyte	Ref.
***w*-$A_{100}H_0$**	–1.3	51.8 ±0.6	6	unchanged	0.1 M $KHCO_3$	This work
[{Cu_3(μ_3-OCH_3)(μ-MePz)$_3$}$_2$(μ-MePz)$_3$(μ_6-Cl)] (**Cu_6**)	–1.0	60.9 ±2.6	3	unchanged	0.5 M KOH	[S8]
[Cu(4-HPz)$_2$] (**Cu-PzH**)	–1.0	56.0 ±4.9	4	unchanged	1 M KOH	[S9]
[Cu(4-ClPz)$_2$] (**Cu-PzCl**)		39.5 ±0.6	N/A	N/A		
[Cu(4-BrPz)$_2$] (**Cu-PzBr**)		31.4 ±2.1	N/A	N/A		
[Cu(4-IPz)$_2$] (**Cu-PzI**)		29.2 ±5.6	3.5	unchanged		
[Cu_3-(μ_3-OH)(μ-pz)$_3$]Br_2 (**Cu_3-Br**)	–0.7	55.0	9.5	unchanged	0.5 M KOH	[S10]
[Cu_3-(μ_3-OH)(μ-pz)$_3$]Cl_2 (**Cu_3-Cl**)	–0.9	47.6	N/A	N/A		
[Cu_3-(μ_3-OH)(μ-pz)$_3$](NO_3)$_2$ (**Cu_3-NO_3**)	–0.8	31.9	N/A	N/A		
[Cu(dmetz)(detz)] (MAF-2ME)	–1.3	47.7 ±2.7	4	unchanged	0.1 M $KHCO_3$	[S1]
[Cu(detz)] (MAF-2E)	–1.3	51.2 ±2.3	8	unchanged		
[Cu(dptz)] (MAF-2P)	–1.3	34.7 ±4.4	8	unchanged		
[Cu_3(μ_3-OH)(μ_3-trz)$_3$(OH)$_2$(H_2O)$_4$] (**Cutrz**)	–1.2	50.6	6	unchanged	0.1 M $KHCO_3$	[S11]
[Cu(PcCu)] (**CuPc-Cu-O**)	–1.2	50	4	unchanged	0.1 M $KHCO_3$	[S12]
[Cu_3(HBtz)$_3$(Btz)Cl_2] (**CuBtz**)	–1.3	44	20	unchanged	0.1 M $KHCO_3$	[S13]
[Cu_4(MeBPZ)$_3$] (**CuBPZ**)	–1.3	43.2	20	unchanged	0.1 M $KHCO_3$	[S14]
$Cu^I_3Cu^{II}_3(NO_3)_3L_3$ (**CuL-1**)	–0.7	31.85	N/A	N/A	1 M KOH	[S15]
[Cu_3(HITP)$_2$] (**CuHITP**)	–1.2	30	10	unchanged	0.1 M $KHCO_3$	[S16]
[Cu_3(Me_4BPz)$_{3/2}$] (NNU-50)	–1.0	14.5	6	unchanged	1 M KOH	[S17]
p-Cu@m-SiO_2	–1.5	56	10	unchanged	1 M KOH	[S18]
Cu@Cu_xO	–1.58	51	10	unchanged	0.1 M $KHCO_3$	[S19]
(*fcc*)Cu	–1.17	46.7	9	unchanged	0.1 M $KHCO_3$	[S20]

Table S6. Series characterization of plane and wavy structures.

Name	***p*-A$_0$H$_{100}$**	***p*-A$_{12}$H$_{88}$**	***p*-A$_{25}$H$_{75}$**	NA	NA	***w*-A$_{25}$H$_{75}$**	***w*-A$_{50}$H$_{50}$**	***w*-A$_{100}$H$_0$**
Parent structure	***p*-A$_0$H$_{100}$**				***w*-A$_{100}$H$_0$**			
Hatz/Htz concentration for exchange (mol L^{-1})	0	0.17	0.33	0.42	0.75	0.67	0.33	0
Structure (confirmed by PXRD)	planar layers			amorphous	amorphous	wavy layers		
atz$^-$/tz$^-$ ratio in structures (confirmed by NMR, %)	0:100	12:88	25:75	29:71	15:85	25:75	50:50	100:0
Morphology (confirmed by TEM)	curved ultrathin nanosheets			NA	NA	curved ultrathin nanosheets		
Thicknesses (confirmed by AFM, nm)	4.5(3)	4.9(2)	4.9(3)	NA	NA	4.5(2)	4.7(2)	4.9(3)
Valence state of Cu (confirmed by XPS)	Cu(I)			NA	NA	Cu(I)		

Table S7. The detail values of faradic efficiency catalyzed by ***p*-$A_{12}H_{88}$**.

First batch (V *vs*. RHE)		CO (%)	CH_4 (%)	C_2H_4 (%)	H_2 (%)	Total (%)
–1.1	Electrode 1	14.8	2.8	2.7	80.6	100.7
	Electrode 2	14.8	3.1	2.7	80.3	100.8
	Electrode 3	13.7	3.8	2.3	78.7	98.4
	Average value	14.4±0.5	3.2±0.4	2.6±0.2	79.8±0.8	100±1.1
–1.2	Electrode 1	14.9	3.8	2.4	80.5	102.0
	Electrode 2	14.5	3.3	2.3	80.1	100.5
	Electrode 3	14.5	4.3	2.6	80.5	101.6
	Average value	14.6±0.2	3.8±0.4	2.4±0.1	80.5±0.3	101.4±0.7
–1.3	Electrode 1	15.5	7.2	2.6	77.5	102.8
	Electrode 2	14.5	7.3	2.0	75.9	99.7
	Electrode 3	14.8	6.5	2.2	75.3	98.8
	Average value	14.9±0.4	7.0±0.4	2.3±0.3	76.2±0.9	80.5±0.3
–1.4	Electrode 1	9.6	8.7	2.2	81.6	102.0
	Electrode 2	9.8	8.8	1.9	79.0	99.5
	Electrode 3	11.6	9.2	1.7	79.3	101.7
	Average value	10.3±0.9	8.9±0.2	1.9±0.2	80.0±1.2	101.1±1.1
–1.5	Electrode 1	7.3	9.3	1.8	81.6	100.0
	Electrode 2	7.9	8.9	1.6	82.9	101.3
	Electrode 3	8.4	9.7	1.5	80.8	100.3
	Average value	7.9±0.4	9.3±0.3	1.6±0.1	81.8±0.9	100.5±0.6
Second batch (V *vs*. RHE)		CO (%)	CH_4 (%)	C_2H_4 (%)	H_2 (%)	Total (%)
–1.1	Electrode 1	14.2	2.9	2.1	79.2	98.4
	Electrode 2	15.3	3.8	3.0	78.6	100.7
	Electrode 3	13.6	3.6	2.7	81.9	101.8
	Average value	14.4±0.9	3.4±0.5	2.6±0.4	79.9±1.5	100.3±1.5
–1.2	Electrode 1	14.7	4.7	2.7	79.5	101.6
	Electrode 2	15.0	5.2	2.6	81.1	103.9
	Electrode 3	15.3	4.8	2.6	80.1	102.8
	Average value	15.0±0.4	4.9±0.2	2.6±0.1	80.3±0.8	102.8±0.9
–1.3	Electrode 1	16.1	7.8	1.9	75.8	101.6
	Electrode 2	15.2	6.4	2.3	78.5	102.3
	Electrode 3	14.9	6.0	2.5	77.5	100.8
	Average value	15.4±0.7	6.7±0.8	2.3±0.4	77.3±1.4	101.6±1.9
–1.4	Electrode 1	9.6	8.7	2.0	80.0	100.2
	Electrode 2	10.4	8.2	2.0	79.2	99.8
	Electrode 3	9.5	8.6	2.0	79.4	99.5
	Average value	9.8±0.4	8.5±0.3	2.0±0.1	79.5±0.8	99.8±0.7
–1.5	Electrode 1	8.5	9.5	1.5	80.4	99.9
	Electrode 2	7.5	9.9	1.7	81.3	100.4
	Electrode 3	7.9	7.9	1.5	80.0	97.3
	Average value	8.0±0.5	9.1±0.9	1.6±0.1	80.6±0.8	99.2±1.5
Third batch (V *vs*. RHE)		CO (%)	CH_4 (%)	C_2H_4 (%)	H_2 (%)	Total (%)
–1.1	Electrode 1	13.5	3.0	2.4	79.8	98.5
	Electrode 2	12.6	3.9	2.8	81.1	100.4
	Electrode 3	12.3	3.3	2.5	80.9	98.9
	Average value	12.8±0.5	3.4±0.4	2.5±0.2	80.6±0.8	99.3±1.2
–1.2	Electrode 1	15.6	5.0	2.6	80.4	103.6
	Electrode 2	16.6	4.5	2.2	80.6	103.9
	Electrode 3	14.4	4.4	2.2	80.1	101.1
	Average value	15.6±1.0	4.6±0.3	2.3±0.2	80.4±0.4	102.9±1.5
–1.3	Electrode 1	15.4	6.0	2.2	76.0	99.6
	Electrode 2	14.8	6.0	2.5	76.9	100.2
	Electrode 3	13.8	6.6	2.6	79.9	102.9
	Average value	14.7±0.7	6.2±0.3	2.4±0.2	77.6±1.7	100.9±1.5
–1.4	Electrode 1	9.9	9.7	1.7	80.8	102.1
	Electrode 2	9.6	9.2	2.0	79.6	100.3
	Electrode 3	8.9	8.1	2.0	79.9	98.7
	Average value	9.5±0.5	9.0±0.7	1.9±0.2	80.1±0.8	100.4±1.6
–1.5	Electrode 1	7.6	9.6	1.5	81.5	100.2
	Electrode 2	7.1	9.5	1.3	80.8	98.7
	Electrode 3	7.2	8.4	1.6	83.7	100.9
	Average value	7.3±0.4	9.2±0.6	1.5±0.1	82.0±1.3	100.0±1.0
Three batch (V *vs*. RHE)		CO (%)	CH_4 (%)	C_2H_4 (%)	H_2 (%)	Total (%)
Average value	–1.1	13.9±0.8	3.3±0.1	2.6±0.1	80.1±0.3	99.9±0.4
	–1.2	15.1±0.4	4.4±0.5	2.5±0.1	80.4±0.1	102.3±0.7
	–1.3	15.0±0.3	6.6±0.3	2.3±0.1	77.0±0.6	101.0±0.5
	–1.4	9.9±0.4	8.8±0.2	1.9±0.1	79.9±0.2	100.4±0.5
	–1.5	7.7±0.3	9.2±0.1	1.6±0.1	81.4±0.6	99.9±0.6

Table S8. The detail values of faradic efficiency catalyzed by ***p*-A$_{25}$H$_{75}$**.

First batch (V *vs.* RHE)		CO (%)	CH_4 (%)	C_2H_4 (%)	H_2 (%)	Total (%)
–1.1	Electrode 1	14.8	3.8	2.9	81.2	102.7
	Electrode 2	16.2	4.2	2.1	78.9	101.4
	Electrode 3	14.9	4.7	3.1	77.7	100.4
	Average value	15.3±0.6	4.2±0.4	2.7±0.5	79.3±1.5	101.5±0.9
–1.2	Electrode 1	15.6	6.3	3.0	78.8	103.8
	Electrode 2	13.4	6.6	2.9	76.6	99.5
	Electrode 3	13.6	6.5	2.8	79.4	102.2
	Average value	14.2±1.0	6.5±0.1	2.9±0.1	78.3±1.2	101.8±1.8
–1.3	Electrode 1	13.6	7.5	2.5	77.4	101.0
	Electrode 2	13.6	7.2	2.5	77.6	100.9
	Electrode 3	12.0	7.6	2.6	77.7	99.8
	Average value	13.1±0.8	7.4±0.2	2.5±0.1	77.6±0.1	100.6±0.5
–1.4	Electrode 1	10.8	8.7	2.1	79.2	100.6
	Electrode 2	10.4	8.4	1.9	78.3	99.0
	Electrode 3	11.3	8.6	2.0	77.2	99.1
	Average value	10.8±0.4	8.6±0.1	2.0±0.1	78.2±0.8	99.6±0.7
–1.5	Electrode 1	7.6	10.0	1.4	81.1	100.1
	Electrode 2	7.9	9.3	1.7	79.2	98.1
	Electrode 3	7.7	10.0	1.7	80.7	100.2
	Average value	7.8±0.1	9.7±0.3	1.6±0.2	80.4±0.8	99.5±1.0
Second batch (V *vs.* RHE)		CO (%)	CH_4 (%)	C_2H_4 (%)	H_2 (%)	Total (%)
–1.1	Electrode 1	15.0	4.7	3.1	77.3	100.1
	Electrode 2	14.1	4.4	2.9	78.2	99.4
	Electrode 3	13.3	5.2	3.1	79.4	101.0
	Average value	14.1±0.8	4.8±0.5	3.0±0.1	78.3±0.9	100.2±0.9
–1.2	Electrode 1	12.7	6.4	2.4	78.5	100.1
	Electrode 2	12.4	6.7	2.9	80.5	102.5
	Electrode 3	11.9	6.5	2.6	78.4	99.4
	Average value	12.4±0.4	6.5±0.2	2.6±0.3	79.1±1.1	100.7±1.4
–1.3	Electrode 1	12.0	7.2	3.0	78.6	100.7
	Electrode 2	11.4	6.9	2.4	79.8	100.5
	Electrode 3	11.7	7.5	2.6	79.1	100.8
	Average value	11.7±0.4	7.2±0.3	2.6±0.4	79.2±0.5	100.7±0.7
–1.4	Electrode 1	10.3	7.8	1.8	78.7	98.6
	Electrode 2	10.5	9.6	2.1	79.7	102.0
	Electrode 3	10.2	8.7	2.0	77.8	98.7
	Average value	10.4±0.2	8.7±0.7	2.0±0.2	78.7±0.8	99.8±1.6
–1.5	Electrode 1	7.4	9.3	1.5	80.5	98.7
	Electrode 2	8.5	9.6	1.6	79.9	99.6
	Electrode 3	7.6	8.8	1.3	82.3	100.0
	Average value	7.8±0.5	9.2±0.4	1.5±0.2	80.9±1.1	99.4±0.8
Third batch (V *vs.* RHE)		CO (%)	CH_4 (%)	C_2H_4 (%)	H_2 (%)	Total (%)
–1.1	Electrode 1	16.1	4.0	2.9	76.6	99.6
	Electrode 2	14.0	4.4	2.9	77.5	98.7
	Electrode 3	15.4	4.5	2.3	77.8	100.1
	Average value	15.2±0.9	4.3±0.3	2.7±0.3	77.3±0.6	99.4±1.0
–1.2	Electrode 1	14.3	6.5	2.7	80.0	103.5
	Electrode 2	13.2	6.5	2.8	78.1	100.6
	Electrode 3	14.2	6.4	2.6	77.9	101.0
	Average value	13.9±0.5	4.7±0.2	2.7±0.2	78.7±1.0	101.7±1.3
–1.3	Electrode 1	12.6	7.5	2.2	76.3	98.7
	Electrode 2	11.8	6.7	2.4	76.1	97.0
	Electrode 3	14.2	7.3	2.4	76.8	100.7
	Average value	12.9±1.0	7.2±0.4	2.3±0.1	76.4±1.1	98.8±1.7
–1.4	Electrode 1	11.0	8.4	2.1	79.8	101.3
	Electrode 2	10.6	8.3	1.9	81.8	102.6
	Electrode 3	10.1	7.7	2.1	78.6	98.4
	Average value	10.6±0.4	8.1±0.4	2.0±0.2	80.0±1.3	100.8±1.7
–1.5	Electrode 1	7.8	9.2	1.6	81.2	99.7
	Electrode 2	7.8	10.3	1.7	80.6	100.4
	Electrode 3	7.5	10.7	2.0	81.5	101.7
	Average value	7.7±0.2	10.1±0.8	1.8±0.2	81.1±0.4	100.6±0.8
Three batch (V *vs.* RHE)		CO (%)	CH_4 (%)	C_2H_4 (%)	H_2 (%)	Total (%)
Average value	–1.1	14.9±0.5	4.4±0.2	2.8±0.2	78.3±0.8	100.4±0.9
	–1.2	13.5±0.8	6.5±0.1	2.7±0.1	78.7±0.3	101.4±0.5
	–1.3	12.5±0.6	7.3±0.1	2.5±0.1	77.0±1.1	100.0±0.9
	–1.4	10.6±0.2	8.5±0.2	2.0±0.1	79.0±0.8	100.0±0.5
	–1.5	7.8±0.1	9.7±0.3	1.6±0.1	80.8±0.3	99.8±0.5

Table S9. The detail values of faradic efficiency catalyzed by ***w*-$A_{25}H_{75}$.**

First batch (V *vs.* RHE)		CO (%)	CH_4 (%)	C_2H_4 (%)	H_2 (%)	Total (%)
–1.1	Electrode 1	20.4	5.2	12.5	63.9	102.0
	Electrode 2	23.9	4.9	12.6	61.4	102.8
	Electrode 3	21.9	4.7	13.2	62.8	102.5
	Average value	22.1±1.4	5.0±0.2	12.8±0.3	62.7±1.0	102.4±0.3
–1.2	Electrode 1	15.9	9.0	16.3	58.8	100.0
	Electrode 2	17.6	9.1	19.1	55.4	101.1
	Electrode 3	15.9	10.2	18.1	57.4	101.7
	Average value	16.5±0.8	9.5±0.6	17.8±1.2	57.2±1.4	100.9±0.7
–1.3	Electrode 1	10.9	12.6	24.5	53.3	101.3
	Electrode 2	12.8	12.9	22.3	52.5	100.6
	Electrode 3	13.0	12.6	22.9	50.4	98.9
	Average value	12.2±1.0	12.7±0.2	23.3±0.9	52.1±1.2	100.2±1.0
–1.4	Electrode 1	6.1	21.4	17.2	57.0	101.6
	Electrode 2	6.0	21.2	16.2	57.5	100.9
	Electrode 3	6.6	19.7	15.1	59.6	101.0
	Average value	6.2±0.3	20.8±0.8	16.2±0.8	58.0±1.2	101.2±0.3
–1.5	Electrode 1	1.9	22.6	4.5	72.7	101.6
	Electrode 2	2.5	22.8	3.3	70.3	98.7
	Electrode 3	2.6	24.7	4.4	69.2	100.9
	Average value	2.3±0.3	23.4±1.0	4.0±0.6	70.7±1.4	100.4±1.2
Second batch (V *vs.* RHE)		CO (%)	CH_4 (%)	C_2H_4 (%)	H_2 (%)	Total (%)
–1.1	Electrode 1	22.8	4.6	12.2	62.6	102.2
	Electrode 2	21.4	4.5	12.8	62.6	101.4
	Electrode 3	18.5	4.8	11.7	65.7	100.7
	Average value	20.9±1.9	4.6±0.2	12.3±1.3	63.6±1.5	101.4±1.0
–1.2	Electrode 1	17.0	10.2	16.9	58.0	102.0
	Electrode 2	17.4	9.2	15.8	59.7	102.1
	Electrode 3	15.9	10.8	18.7	56.8	102.2
	Average value	16.8±0.7	10.0±0.7	17.1±1.2	58.2±1.2	102.1±0.6
–1.3	Electrode 1	13.5	10.2	16.9	58.0	98.6
	Electrode 2	11.7	15.3	22.8	51.0	100.7
	Electrode 3	11.3	13.7	23.3	52.4	100.7
	Average value	12.2±1.0	13.1±2.2	21.0±3.1	53.8±3.1	100.0±1.1
–1.4	Electrode 1	6.4	21.1	16.3	60.0	103.8
	Electrode 2	6.8	22.6	16.6	56.2	102.1
	Electrode 3	6.2	21.9	15.8	57.0	100.9
	Average value	6.45±0.33	21.86±0.64	16.23±0.36	57.74±1.64	102.28±1.38
–1.5	Electrode 1	2.2	24.3	3.4	66.6	96.4
	Electrode 2	2.5	25.4	5.5	64.6	98.0
	Electrode 3	3.5	24.3	5.0	64.8	97.5
	Average value	2.69±0.57	24.67±0.53	4.61±0.90	65.33±0.97	97.30±0.75
Third batch (V *vs.* RHE)		CO (%)	CH_4 (%)	C_2H_4 (%)	H_2 (%)	Total (%)
–1.1	Electrode 1	19.0	5.9	11.7	66.4	103.0
	Electrode 2	19.2	5.7	11.1	64.6	100.6
	Electrode 3	20.1	4.2	12.6	64.5	101.4
	Average value	19.4±0.5	5.3±0.8	11.8±0.6	65.2±1.1	101.6±1.2
–1.2	Electrode 1	17.2	9.0	17.8	57.6	101.6
	Electrode 2	17.3	9.8	18.5	55.7	101.3
	Electrode 3	17.4	8.9	18.0	59.2	103.5
	Average value	17.3±0.2	9.2±0.6	18.1±0.8	57.5±1.5	102.1±1.1
–1.3	Electrode 1	12.9	12.0	23.5	51.0	99.4
	Electrode 2	14.2	12.5	23.9	47.9	98.5
	Electrode 3	14.3	11.4	22.3	51.8	99.9
	Average value	13.8±0.8	12.0±0.6	23.3±0.9	50.2±1.8	99.3±1.3
–1.4	Electrode 1	6.5	20.3	14.2	56.5	97.5
	Electrode 2	6.4	21.8	13.8	57.3	99.3
	Electrode 3	6.0	20.8	13.3	58.9	99.0
	Average value	6.3±0.6	21.0±0.7	13.8±0.4	57.6±1.1	98.6±1.4
–1.5	Electrode 1	2.3	25.8	5.4	64.2	97.8
	Electrode 2	3.1	24.5	5.8	66.9	100.2
	Electrode 3	3.5	25.9	5.5	63.3	98.2
	Average value	3.0±0.5	25.4±0.7	5.6±0.2	64.8±1.5	98.7±1.2
Three batch (V *vs.* RHE)		CO (%)	CH_4 (%)	C_2H_4 (%)	H_2 (%)	Total (%)
Average value	–1.1	20.8±1.1	4.9±0.3	12.3±0.4	63.8±1.0	101.8±0.4
	–1.2	16.8±0.4	9.6±0.4	17.7±0.4	57.6±0.4	101.7±0.6
	–1.3	12.7±0.8	12.6±0.4	22.5±1.1	52.0±1.5	99.8±0.4
	–1.4	6.3±0.1	21.2±0.5	15.4±1.2	57.8±0.2	100.7±1.5
	–1.5	2.7±0.3	24.5±0.8	4.7±0.6	66.9±2.7	98.8±1.3

Table S10. The detail values of faradic efficiency catalyzed by ***w*-A$_{50}$H$_{50}$.**

First batch (V *vs.* RHE)		CO (%)	CH_4 (%)	C_2H_4 (%)	H_2 (%)	Total (%)
–1.1	Electrode 1	19.0	11.6	17.9	51.7	100.2
	Electrode 2	16.7	10.7	17.1	51.5	95.9
	Electrode 3	15.6	12.7	23.9	50.8	102.9
	Average value	17.1±1.41	11.7±0.8	19.6±3.1	51.3±0.4	99.7±2.3
–1.2	Electrode 1	14.7	10.6	31.0	43.4	99.6
	Electrode 2	15.4	11.6	30.5	41.3	98.8
	Electrode 3	16.9	10.6	27.7	42.3	97.5
	Average value	15.7±1.0	10.9±0.5	29.7±1.5	42.3±0.9	98.7±0.9
–1.3	Electrode 1	11.3	12.6	32.5	43.2	99.5
	Electrode 2	13.2	12.4	31.9	42.2	99.7
	Electrode 3	12.1	12.9	35.7	38.6	99.4
	Average value	12.2±0.8	12.7±0.2	33.4±1.7	41.3±2.0	99.5±0.1
–1.4	Electrode 1	3.6	26.4	18.7	48.7	97.5
	Electrode 2	4.2	27.1	19.2	48.5	98.9
	Electrode 3	5.2	27.7	18.6	50.6	102.2
	Average value	4.3±0.7	27.1±0.5	18.9±0.3	49.3±1.0	99.5±2.0
–1.5	Electrode 1	2.1	31.9	11.9	52.8	98.7
	Electrode 2	4.1	35.6	11.9	48.1	99.8
	Electrode 3	4.8	35.1	11.7	49.7	101.3
	Average value	3.7±1.2	34.2±1.6	11.8±0.1	50.2±2.0	99.9±1.1
Second batch (V *vs.* RHE)		CO (%)	CH_4 (%)	C_2H_4 (%)	H_2 (%)	Total (%)
–1.1	Electrode 1	18.4	11.0	17.4	50.7	97.4
	Electrode 2	19.5	12.1	19.1	49.1	99.8
	Electrode 3	16.5	12.2	18.9	51.9	99.5
	Average value	18.1±1.2	11.8±0.6	18.5±0.8	50.6±1.7	98.9±1.8
–1.2	Electrode 1	17.6	11.1	30.7	39.8	99.3
	Electrode 2	19.8	7.8	30.0	43.0	100.6
	Electrode 3	15.2	10.7	30.3	46.0	102.2
	Average value	17.5±2.0	9.9±1.7	30.3±0.7	43.0±2.5	100.7±1.3
–1.3	Electrode 1	13.1	13.7	35.4	36.2	98.4
	Electrode 2	13.4	12.7	32.4	37.2	95.7
	Electrode 3	11.0	19.2	31.8	39.6	101.5
	Average value	12.5±1.1	15.2±2.8	33.2±1.6	37.7±1.5	98.5±2.5
–1.4	Electrode 1	5.7	26.3	16.7	47.6	96.3
	Electrode 2	6.6	27.5	15.3	50.1	99.4
	Electrode 3	4.4	23.6	19.7	47.7	95.5
	Average value	5.5±0.9	25.8±1.6	17.2±2.0	48.5±1.2	97.1±2.4
–1.5	Electrode 1	5.2	34.1	12.3	49.1	100.6
	Electrode 2	5.8	33.7	11.4	47.7	98.5
	Electrode 3	5.9	34.5	12.4	49.1	101.8
	Average value	5.6±0.4	34.1±0.5	12.0±0.5	48.6±0.7	100.3±1.4
Third batch (V *vs.* RHE)		CO (%)	CH_4 (%)	C_2H_4 (%)	H_2 (%)	Total (%)
–1.1	Electrode 1	17.6	11.1	17.5	54.6	100.7
	Electrode 2	18.5	10.6	19.4	51.1	99.5
	Electrode 3	16.2	10.3	17.2	54.3	97.9
	Average value	17.4±0.9	10.7±1.0	18.0±1.3	53.3±1.6	99.4±1.5
–1.2	Electrode 1	15.3	10.5	26.7	46.9	99.3
	Electrode 2	16.3	9.0	31.0	42.5	98.8
	Electrode 3	20.4	12.2	29.9	39.1	101.5
	Average value	17.4±2.2	10.6±1.52	29.2±2.5	42.8±3.6	99.9±2.7
–1.3	Electrode 1	12.5	12.9	31.2	43.7	100.2
	Electrode 2	14.3	12.5	32.2	39.5	98.5
	Electrode 3	10.6	9.6	35.5	38.5	94.1
	Average value	12.5±1.6	11.6±1.6	32.9±1.9	40.6±2.2	97.6±2.6
–1.4	Electrode 1	7.7	26.4	18.8	48.8	101.7
	Electrode 2	5.3	29.1	16.3	50.5	101.2
	Electrode 3	6.6	23.9	13.8	51.6	95.8
	Average value	6.5±1.0	26.5±2.2	16.3±2.1	50.3±1.1	99.6±2.7
–1.5	Electrode 1	6.1	34.1	13.0	49.4	102.6
	Electrode 2	6.1	32.9	10.2	51.7	100.9
	Electrode 3	6.4	33.7	11.6	51.4	103.1
	Average value	6.2±0.2	33.6±0.5	11.6±1.1	50.8±1.0	102.2±1.0
Three batch (V *vs.* RHE)		CO (%)	CH_4 (%)	C_2H_4 (%)	H_2 (%)	Total (%)
Average value	–1.1	17.5±0.5	11.4±0.5	18.7±0.7	51.7±1.2	99.3±0.3
	–1.2	16.9±0.8	10.5±0.4	29.8±0.5	42.7±0.3	99.8±0.8
	–1.3	12.4±0.1	13.2±1.5	33.2±0.2	39.8±1.6	98.5±0.8
	–1.4	5.5±0.9	26.5±0.5	17.5±1.1	49.3±0.8	98.7±1.2
	–1.5	5.2±1.1	33.9±0.3	11.8±0.2	49.9±0.9	100.8±1.0

References:

S1 L. L. Zhuo, P. Chen, K. Zheng, X. W. Zhang, J. X. Wu, D. Y. Lin, S. Y. Liu, Z. S. Wang, J. Y. Liu, D. D. Zhou and J. P. Zhang, *Angew. Chem. Int. Ed.*, 2022, **61**, e202204967.

S2 P. J. Pedew, K. Burke and M. Ernzerhof, *Phys*. *Rev. Lett*., **1996**, 77, 3865.

S3 A. Tkatchenko and M. Scheffler, *Phys. Rev. Lett.*, **2009**, *102*, 073005.

S4 X. Guan, C. X. Zhao, X. P. Liu, S. Liu, W. Gao and Q .Jiang, *J. Phys. Chem. C*, **2020**, *124*, 25898.

S5 S. J. Fu, X. Liu, J. R. Ran, Y. Jiao, *Catal. Today,* **2022***, 397,* 574.

S6 J.-P. Zhang, Y.-Y. Lin, X.-C. Huang and X.-M. Chen, *J. Am. Chem. Soc.*, 2005, **127**, 5495.

S7 D. Chen, Y.-J. Liu, Y.-Y. Lin, J.-P. Zhang and X.-M. Chen, *CrystEngComm*, 2011, **13**, 3827.

S8 R. Wang, J. Liu, L.-Z. Dong, J. Zhou, Q. Huang, Y.-R. Wang, J.-W. Shi and Y.-Q. Lan, *CCS Chem.*, 2023, **5**, 2237.

S9 R. Wang, J. Liu, Q. Huang, L. Z. Dong, S. L. Li and Y. Q. Lan, *Angew. Chem. Int. Ed.*, 2021, **60,** 19829.

S10 Y. F. Lu, L. Z. Dong, J. Liu, R. X. Yang, J. J. Liu, Y. Zhang, L. Zhang, Y. R. Wang, S. L. Li and Y. Q. Lan, *Angew. Chem. Int. Ed.*, 2021, **60**, 26210.

S11 D.-S. Huang, H.-L. Zhu, Z.-H. Zhao, J.-R. Huang, P.-Q. Liao and X.-M. Chen, *ACS Catal.*, 2022, **12**, 8444.

S12 X.-F. Qiu, H.-L. Zhu, J.-R. Huang, P.-Q. Liao and X.-M. Chen, *J. Am. Chem. Soc.*, 2021, **143**, 7242.

S13 H.-L. Zhu, J.-R. Huang, P.-Q. Liao and X.-M. Chen, *ACS Cent. Sci*., 2022, **8**, 1506.

S14 Y. Y. Liu, Z. S. Wang, P. Q. Liao and X. M. *Chem–Asian J*., 2022, **17**. e202200764.

S15 J.-N. Lu, J. Liu, L. Zhang, L.-Z. Dong, S.-L. Li and Y.-Q. Lan, *J. Mater. Chem. A*, 2021, **9**, 23477.

S16 Z.-H. Zhao, H.-L. Zhu, J.-R. Huang, P.-Q. Liao and X.-M. Chen, *ACS Catal.*, 2022, **12**, 7986.

S17 L.-Z. Dong, Y.-F. Lu, R. Wang, J. Zhou, Y. Zhang, L. Zhang, J. Liu, S.-L. Li and Y.-Q. Lan, *Nano Res*., 2022, **15**, 10185.

S18 W.-F. Xiong, D.-H. Si, H.-F. Li, X. Song, T. Wang, Y.-B. Huang, T.-F. Liu, T. Zhang and R. Cao, *J. Am. Chem. Soc.*, 2024, **146**, 289.

S19 K. Yao, Y. Xia, J. Li, N. Wang, J. Han, C. Gao, M. Han, G. Shen, Y. Liu, A. Seifitokaldani, X. Sun and H. Liang, *J. Mater. Chem. A*, 2020, **8**, 11117.

S20 Y. Chen, Z. Fan, J. Wang, C. Ling, W. Niu, Z. Huang, G. Liu, B. Chen, Z. Lai, X. Liu, B. Li, Y. Zong, L. Gu, J. Wang, X. Wang and H. Zhang, *J. Am. Chem. Soc.*, 2020, **142**, 12760.